

Mantis: A Simulation-Grounded Foundation Model for Disease Forecasting

Carson Dudley*, Reiden Magdaleno, Christopher Harding, Ananya Sharma,
Emily Martin, Marisa Eisenberg

November 4, 2025

Abstract

Infectious disease forecasting in novel outbreaks or low-resource settings is hampered by the need for disease-specific data, bespoke training, and expert tuning. We introduce Mantis, a foundation model trained entirely on mechanistic simulations, which enables out-of-the-box forecasting across diseases, regions, and outcomes, even in settings with limited historical data. We evaluated Mantis against 48 forecasting models across six diseases with diverse transmission modes, assessing both point forecast accuracy (mean absolute error) and probabilistic performance (weighted interval score and coverage). Despite using no real-world data during training, Mantis achieved lower mean absolute error than all models in the CDC’s COVID-19 Forecast Hub when backtested on early pandemic forecasts. Across all other diseases tested, including respiratory, vector-borne, and waterborne pathogens, Mantis consistently ranked in the top two models across all evaluation metrics. Notably, Mantis generalized to diseases with transmission mechanisms not represented in its training data, demonstrating that it captures fundamental contagion dynamics rather than memorizing disease-specific patterns. These capabilities position Mantis as a practical foundation for disease forecasting: general-purpose, accurate, and deployable where traditional models fail.

Introduction

Accurate forecasting of infectious disease dynamics is fundamental to effective public health response. During the COVID-19 pandemic, forecasts touched nearly every aspect of daily life—from how scarce hospital beds were allocated to if restaurants could open and whether families could send their children to school [1]. Yet despite their importance, disease forecasts often fail in practice, particularly when they are most needed. During the first two years of the COVID-19 pandemic, the performance of many models in the CDC Forecast Hub was worse than a naïve baseline that simply projected the most recent value forward [2]. This highlights a key limitation of many operational systems: they struggle to provide accurate, actionable forecasts precisely when uncertainty is highest and decisions are most urgent.

Several structural limitations contribute to this breakdown. First, most models require large volumes of disease-specific historical data, which are rarely available early in outbreaks. Second, they rely on extensive manual tuning by expert teams, limiting scalability and access in under-resourced health departments, such as those in rural counties or low- and middle-income countries. Third, they generalize poorly across diseases, locations, or targets, necessitating new models for every context. In addition, their forecasting horizons are typically short: most models only predict 1–4 weeks ahead [2, 3, 4], far too short-term for real-world public health planning. Key decisions, such as ramping up hospital capacity, acquiring ventilators, or coordinating vaccination campaigns, often require 6–8 weeks of lead time. Without reliable long-range forecasts, these decisions are either delayed or made reactively, often at considerable cost [5].

Typically, projections beyond 4 weeks are restricted to scenario analysis, which explores hypothetical outcomes conditional on specific policy interventions or behavioral changes [6, 7]. However, unconditional

* Corresponding author, cdud@umich.edu

forecasts at longer horizons remain valuable for public health planning. We define forecasts as unconditional projections of expected outcomes, versus scenario analyses that specify hypothetical interventions. By this definition, temporal horizon does not determine whether a projection is a forecast or a scenario—an 8-week unconditional projection is a forecast, while a 2-week conditional projection is still scenario analysis. Public health decisions such as hospital capacity expansion and vaccination campaigns often require 6-8 weeks of lead time, motivating the development of models capable of reliable longer-range forecasting without any policy assumptions.

Addressing these challenges (limited historical data, poor cross-disease generalization, restricted forecast horizons, and the need for extensive expert tuning) requires a different approach to model training. Simulation-Grounded Neural Networks (SGNNs) provide such a framework [8]. SGNNs learn entirely from large-scale, highly realistic mechanistic simulations, using data generated by domain-specific simulators to train flexible neural networks. In epidemiology, this means generating synthetic outbreaks from mechanistic disease models that capture processes such as transmission, progression, immunity, seasonality, and intervention effects, then training models on these simulated trajectories so they can forecast real-world outbreaks they have never encountered before. By grounding learning in simulated systems that encode known mechanisms—whether physical, biological, or social—SGNNs enable models to generalize to real-world settings where data are limited, noisy, or missing.

We present Mantis, the first large-scale foundation model built on the SGNN paradigm. Building on early demonstrations of simulation-grounded forecasting [9], Mantis is trained entirely on mechanistic simulations without access to any real-world training data. It learns from over 400 million simulated days of outbreak dynamics spanning diverse pathogens, transmission routes (human-to-human, vector-borne, environmental), intervention strategies, immunity profiles, and surveillance artifacts such as underreporting and delays. These simulations encode core epidemiological mechanisms, allowing Mantis to internalize generalizable contagion dynamics rather than extrapolating from historical trends. Unlike traditional models, Mantis requires no disease-specific tuning or retraining, yet it produces accurate probabilistic forecasts out-of-the-box across diseases, geographies, and targets (Figure 1).

We evaluate Mantis against 48 models across forecasting tasks spanning six real-world diseases: seasonal influenza, early COVID-19, dengue, hepatitis B, smallpox, and scarlet fever. These evaluations cover multiple transmission modes, outbreak phases, surveillance systems, and historical eras. We assessed both point forecast accuracy and probabilistic performance. When benchmarked against CDC Forecast Hub models on early pandemic COVID-19 forecasts, Mantis achieved the lowest mean absolute error despite using no COVID-specific data or covariates in training and was tied for the second lowest weighted interval score. Across all other diseases—including those with transmission mechanisms absent from its training data—Mantis consistently ranked among the top two models on all evaluation metrics, demonstrating robust generalization to diverse epidemiological settings.

These capabilities establish Mantis as a general-purpose forecasting system offering a scalable solution for modeling in data-scarce or rapidly evolving settings. To support deployment, we release Mantis as an open-source repository. Users can generate forecasts from a single historical time series without any machine learning expertise.¹ Mantis is currently contributing forecasts to a new local-scale forecasting hub within Michigan for the 2025-2026 respiratory virus season and will be submitted to the CDC Forecast Hub to support real-time public health decision-making.

Results

We assessed Mantis’s forecasting accuracy across a set of real-world forecasting tasks spanning six diseases: seasonal influenza [10, 11], early COVID-19 [12], dengue [13], hepatitis B [14], smallpox [15], and scarlet fever [16]. For each task, we benchmarked Mantis against expert-tuned statistical and machine learning models, including published baselines and submissions to the CDC COVID-19 Forecast Hub [2] (see Methods). We evaluated both point forecast accuracy using mean absolute error (MAE) and probabilistic forecasting performance using weighted interval score (WIS) and coverage metrics (e.g., how often did the 95% CI actually contain the true value).

¹github.com/carsondudley1/Mantis: Pretrained models, example data, and an interactive forecasting demo are available.

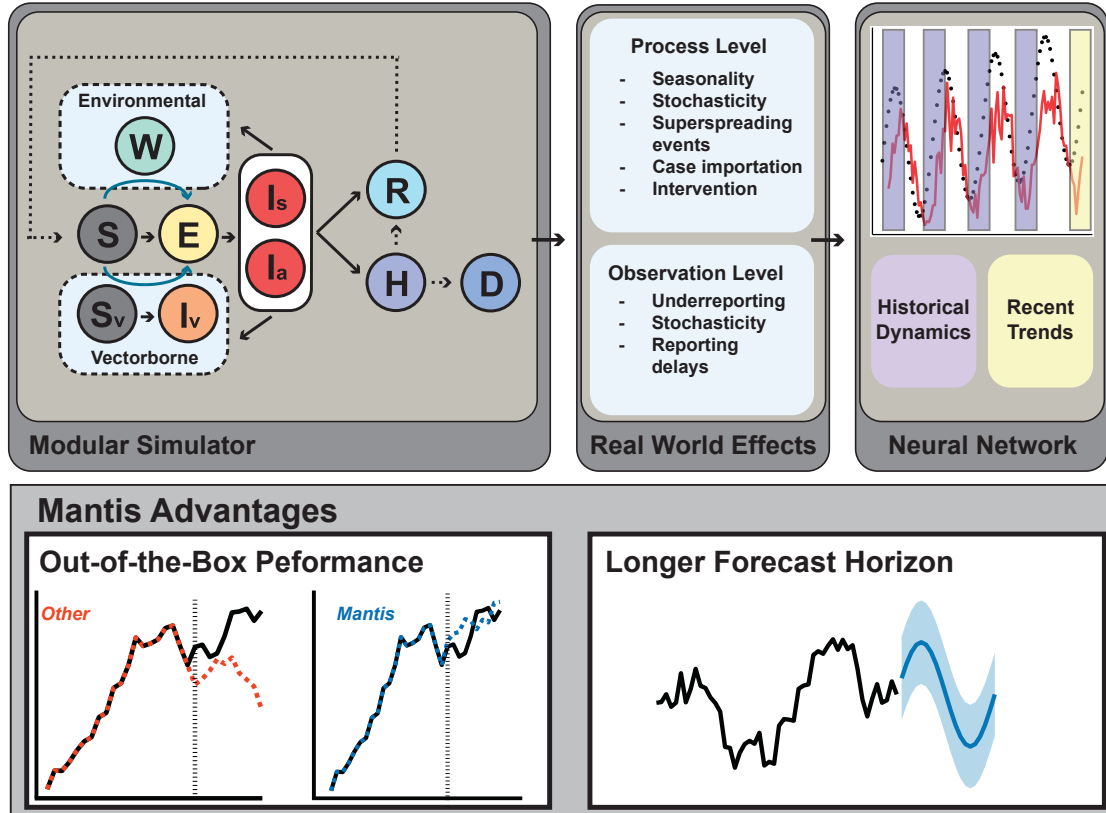


Figure 1: **Conceptual overview of Mantis.** Mantis is a simulation-grounded foundation model trained entirely on synthetic outbreaks generated by mechanistic epidemiological models. The training pipeline begins with a modular simulator that encodes diverse outbreak mechanisms, including multiple transmission modes (human-to-human, vectorborne, environmental), progression dynamics, intervention strategies, and population structures. These simulations are then passed through an observation model that incorporates real-world surveillance effects such as underreporting, stochasticity, and reporting delays. Trained on over 400 million simulated days, Mantis forecasts directly from real-world time series at inference time. Key advantages include accurate out-of-the-box performance, long-range forecasting capability, and mechanistic interpretability via back-to-simulation attribution.

Mantis Achieves Competitive Performance Across Diseases and Tasks

For each disease, we evaluated performance across multiple spatial and temporal resolutions, including U.S. states and smaller regions within states. We evaluated both point forecast performance (mean absolute error, MAE) and probabilistic metrics (weighted interval score, WIS; 50% and 95% coverage). WIS is the standard probabilistic evaluation metric for disease forecasting [17], providing a comprehensive assessment that accounts for both forecast accuracy and uncertainty calibration across predicted quantiles. Following the evaluation framework established in [2], we report relative MAE and relative WIS, where metrics are normalized by the performance of a naïve baseline that forecasts the current value forward with uncertainty intervals derived from historical variance (see Methods). Relative metrics offer two key advantages over absolute error: they provide an interpretable measure of the information contributed by a model beyond simple persistence, and they enable meaningful comparisons across different forecast targets and geographic scales, where absolute case or death counts may vary by orders of magnitude.

We compare Mantis against a range of published and re-implemented models, including top submissions to the CDC COVID-19 Forecast Hub, statistical baselines (exponential smoothing and SARIMA), LSTM neural networks retrained at each forecast point, and Chronos, a state-of-the-art time-series foundation model

[18].

Mantis achieved competitive performance across diseases and metrics (Table 1). For early pandemic COVID-19 forecasts at the state level, Mantis achieved the lowest MAE among evaluated models, including the CDC Forecast Hub ensemble that combines dozens of expert-tuned submissions. The CDC ensemble achieved slightly better WIS (0.61 vs 0.63), while UMass-MechBayes achieved marginally better 95% coverage (0.93 vs 0.91), demonstrating that multiple approaches can excel on different aspects of probabilistic forecasting. Although results have shown that some general time series forecasting foundation models can confer reasonable results for infectious disease forecasting [19], we did not find that any we tested gave competitive performance with Mantis or our other baseline models, so we did not include them in our analysis.

Across the five additional diseases tested—*influenza hospitalizations, dengue, smallpox, scarlet fever, and hepatitis B*—Mantis consistently ranked first or second on both point forecast accuracy (MAE) and probabilistic performance (WIS).

Example forecast trajectories illustrate Mantis’s ability to match the timing and magnitude of real-world outbreaks across diverse epidemiological settings (Figure 3). Forecasts include uncertainty intervals derived from the model’s predicted quantiles, enabling direct use in probabilistic planning. Because Mantis is trained entirely on broad mechanistic simulations rather than historical observations, it requires no model fitting or fine-tuning for new targets.

Covariates Improve Forecast Accuracy Across Horizons

We evaluated two variants of Mantis to assess the impact of additional information on forecasting performance: a covariate-free version, which receives only the time series to be forecast (e.g., deaths), and a covariate-aware version, which also receives related signals (e.g., cases or hospitalizations). This design mirrors real-world forecasting settings, where models may have access to upstream indicators with predictive value. (See Methods for training details for each model.)

For example, when forecasting COVID-19 deaths, the covariate-aware Mantis version receives both historical deaths and upstream case data, while the covariate-free version sees only the death time series. Both models use identical architecture and training data; the only difference is the presence or absence of additional input channels.

Across forecast horizons (2, 4, 6, and 8 weeks), the covariate-aware version consistently outperformed its covariate-free counterpart (Figure 2a), achieving lower mean absolute error across diseases and targets. These improvements were particularly pronounced at longer horizons, where upstream indicators (e.g., cases leading to hospitalizations, then deaths) provide early signals that improve downstream predictions.

These results highlight the benefit of incorporating complementary epidemiological signals when available and demonstrate that Mantis can flexibly leverage additional information without retraining. In data-rich settings, covariate-aware forecasts yield improved performance; in low-data contexts, the covariate-free version retains strong out-of-the-box accuracy, making both variants useful in practice depending on context and data availability.

Mantis Enables Accurate Forecasts at Longer Horizons

We evaluated Mantis’s long-range forecasting performance at an 8-week horizon across the same benchmark tasks and baselines described above. Mantis consistently achieved the lowest relative MAE across all diseases and targets tested, demonstrating its ability to extrapolate epidemiological dynamics further into the future than prior models. At the 8-week horizon, Mantis achieved lower relative error than all models in the CDC Forecast Hub at 4 weeks, and lower raw error than the median 4-week error of Forecast Hub models, demonstrating long-range accuracy that exceeds the short-term limits of existing expert-tuned systems.

Visual examples of 8-week forecasts are shown in figure 3b. Prediction intervals widen with time (figure 2b), maintaining calibrated uncertainty that reflects forecast difficulty (calibration results in table 1).

This capability is not enabled by manual tuning or disease-specific details, but by scale: Mantis learns from millions of simulated outbreak trajectories, encompassing diverse transmission patterns and intervention regimes. Unlike historically trained models, which rely on narrow slices of observed data, simulation-trained models like Mantis can internalize general patterns that support long-range prediction.

Table 1: Forecasting results across diseases and models. For each metric, the best model is highlighted in **green and bold**, and the second-best is blue and underlined.

Disease	Model	Relative MAE	Relative WIS	50% coverage	95% coverage
State-level COVID	Mantis	0.65	<u>0.63</u>	0.51	<u>0.91</u>
	CDC ensemble	<u>0.66</u>	0.61	<u>0.53</u>	0.90
	UMass-MechBayes	0.67	<u>0.63</u>	0.56	0.93
	GT-DeepCOVID	0.82	0.75	0.41	0.84
	UCSD_NEU-DeepGLEAM	0.78	0.83	0.70	<u>0.91</u>
	SARIMA	1.08	1.10	0.44	0.81
	LSTM	1.37	1.54	0.33	0.70
Local-scale flu hosp.	Mantis	0.85	0.86	0.51	0.92
	ETS	1.15	1.32	0.39	0.78
	LSTM	1.21	1.33	0.40	<u>0.79</u>
	SARIMA	<u>1.10</u>	<u>1.00</u>	<u>0.47</u>	0.78
Dengue cases	Mantis	0.75	0.80	0.47	<u>0.90</u>
	ETS	0.99	<u>1.04</u>	<u>0.45</u>	<u>0.90</u>
	LSTM	1.34	1.62	0.37	0.73
	SARIMA	<u>0.94</u>	1.58	0.73	0.92
Smallpox cases	Mantis	0.83	0.84	<u>0.45</u>	<u>0.87</u>
	ETS	1.00	1.06	0.44	0.86
	LSTM	1.31	1.52	0.33	0.71
	SARIMA	<u>0.95</u>	<u>1.04</u>	0.53	0.88
ILI syndromic	Mantis	0.83	0.88	0.46	0.89
	ETS	<u>1.00</u>	1.05	0.43	0.83
	LSTM	1.19	1.30	0.41	0.80
	SARIMA	1.03	<u>0.97</u>	<u>0.45</u>	<u>0.88</u>
Scarlet Fever cases	Mantis	0.80	0.81	0.47	0.91
	ETS	0.89	<u>0.95</u>	<u>0.46</u>	0.89
	LSTM	<u>0.87</u>	1.04	0.36	0.80
	SARIMA	1.05	1.08	0.56	<u>0.90</u>
Hepatitis B cases	Mantis	<u>0.85</u>	0.84	0.47	<u>0.90</u>
	ETS	0.86	<u>0.89</u>	<u>0.46</u>	0.88
	LSTM	0.82	1.07	0.37	0.78
	SARIMA	0.86	0.84	0.58	0.91

Mantis as a Foundation Model: Generalizing to New Mechanisms and Inputs

We next evaluated Mantis’s out-of-the-box forecasting capacity across both held-out transmission mechanisms and new input data modalities.

First, we benchmarked Mantis on diseases governed by transmission and progression mechanisms never

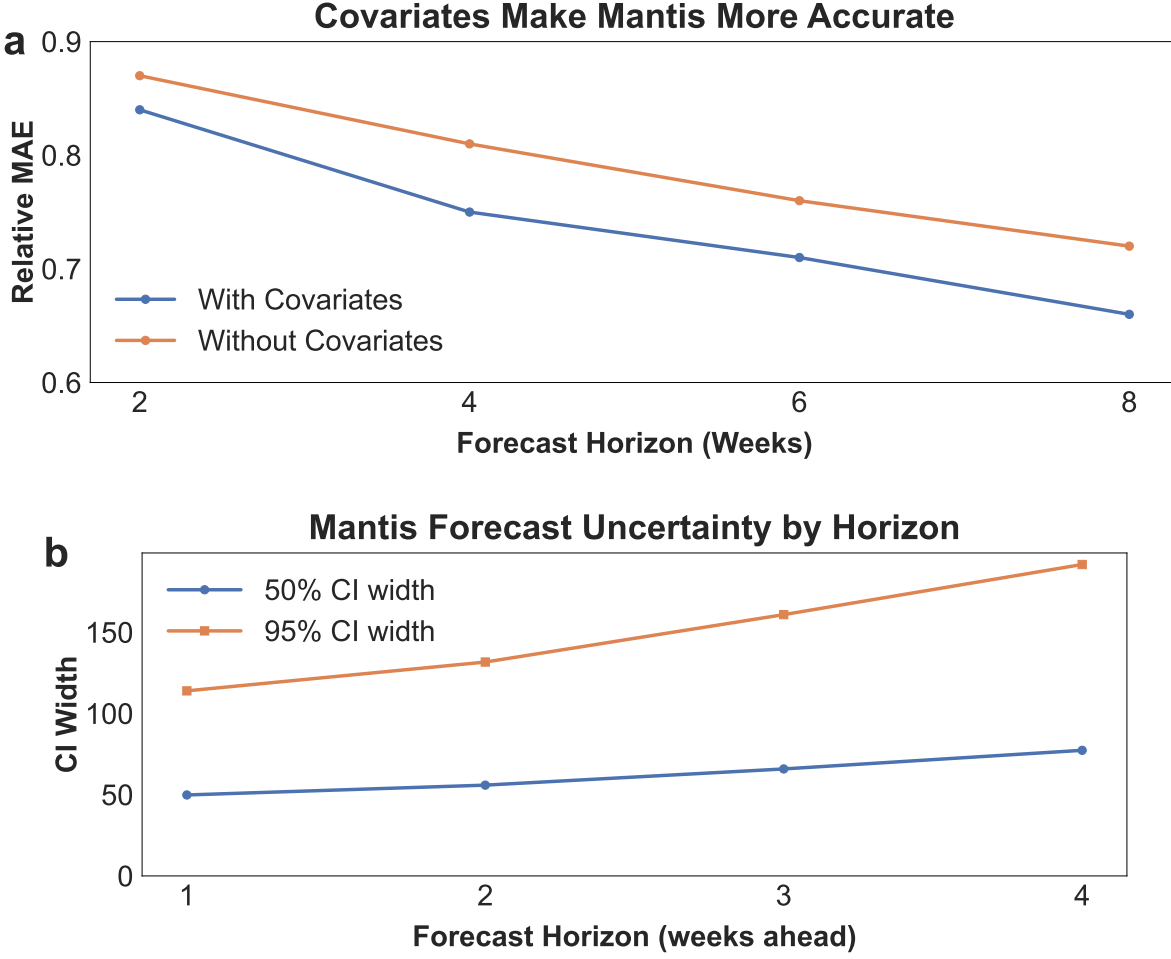


Figure 2: Covariate integration improves accuracy. Mantis maintains calibrated uncertainty across forecast horizons. (a) Including covariates (e.g., using cases to predict hospitalizations) consistently improves Mantis’s accuracy across all forecast horizons. Relative MAE shown for COVID-19 mortality forecasts with (blue) and without (orange) hospitalization covariates across 2, 4, 6, and 8-week horizons. (b) Mantis’s prediction interval widths increase appropriately with forecast horizon, reflecting growing uncertainty in longer-range predictions. The 50% confidence interval width (blue) grows from approximately 50 to 80 deaths, while the 95% interval width (orange) expands from approximately 110 to 180 deaths over 1 to 4 weeks ahead when forecasting COVID-19 mortality. This systematic widening demonstrates the model becoming appropriately less confident as prediction horizon increases.

represented in training simulations. For example, hepatitis B exhibits bloodborne transmission and chronic infection dynamics that are markedly different from the acute, self-limiting outbreaks used in pretraining. The Mantis training set included no models without recovery—all simulated diseases eventually transition out of the infectious state—and the longest average infectious period is just 10 days. In contrast, hepatitis B infection can persist for years. Despite this fundamental mechanistic mismatch, Mantis achieved competitive performance on hepatitis B forecasts, ranking second in MAE (0.85 vs 0.82) and achieving the best WIS (0.84) among all models (Table 1). These results demonstrate that Mantis can generalize across fundamental mechanistic boundaries—not just to new pathogens, but to qualitatively different epidemic regimes, such as chronic persistence versus outbreak spread.

Next, we tested Mantis’s ability to generalize across data modalities. Although trained using cases, hospitalizations, and deaths, Mantis can incorporate new input types at inference time. We evaluated Mantis on syndromic surveillance data (percent of outpatient visits for influenza-like illness), a data type

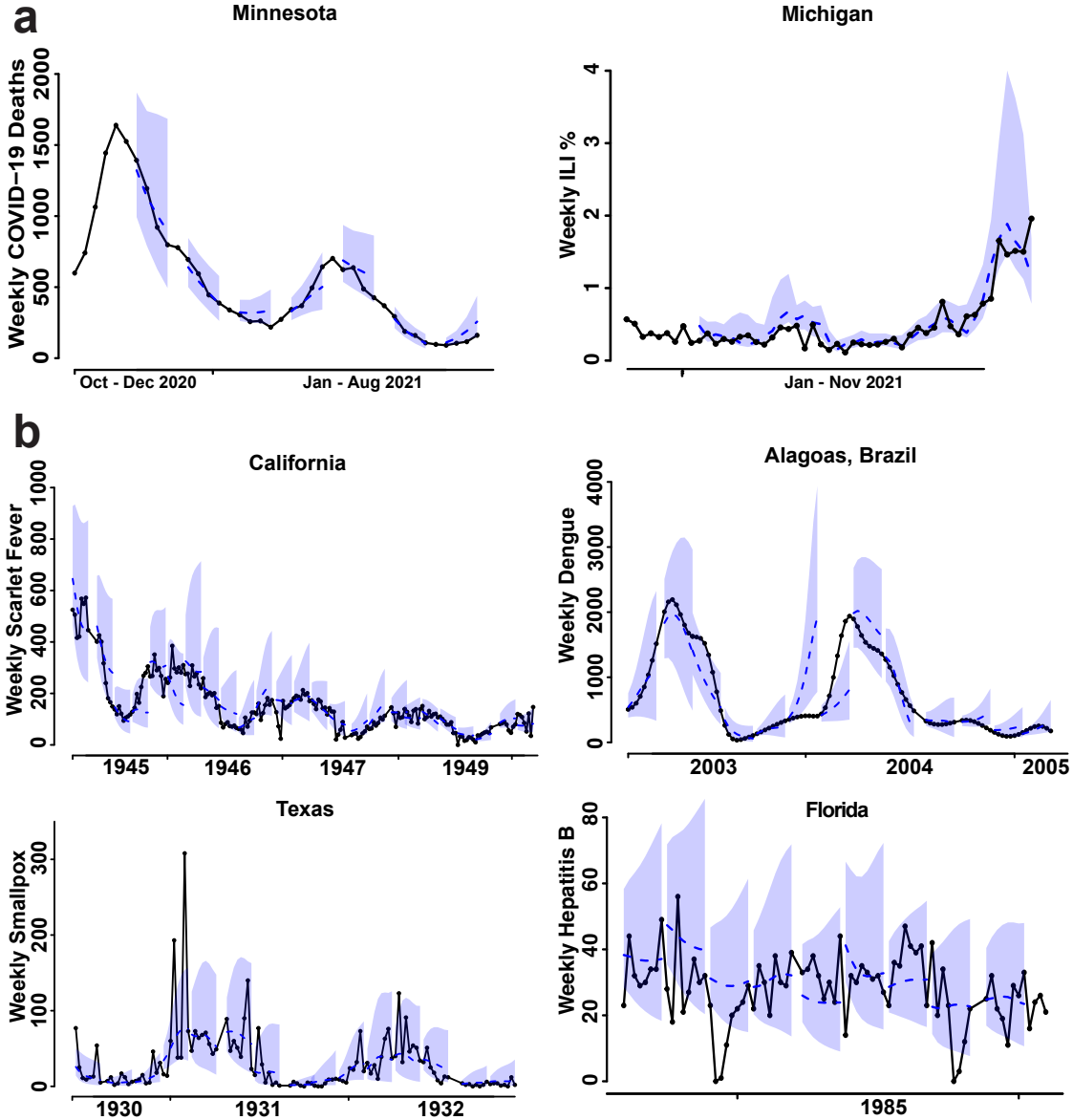


Figure 3: Mantis Produces Accurate and Generalizable Forecasts Across Diseases and Geographies. (a) Four-week-ahead forecasts (blue dashed line and shaded 90% CI) compared to observed outcomes (black) for COVID-19 mortality in Minnesota and influenza-like illness (ILI) in Michigan. In the latter, Mantis demonstrates its foundation model capacity by accurately forecasting syndromic inputs despite never being trained with syndromic data. (b) Eight-week-ahead forecasts for four historical outbreaks, highlighting Mantis’s ability to generalize across time, space, and transmission mode. In Alagoas, Brazil, Mantis forecasts the 2004 dengue surge prematurely, highlighting a failure in temporal calibration due to the absence of covariates, but still estimates the peak height with remarkable accuracy despite being 18 weeks early. Forecasts for hepatitis B in Florida—a chronic, bloodborne disease type absent from Mantis’s training set—further demonstrate its capacity to generalize to out-of-distribution disease profiles while maintaining forecast stability and accuracy.

never represented in training simulations. Despite this distribution shift, Mantis achieved the lowest MAE (0.83) and WIS (0.88) on ILI forecasting (Table 1), demonstrating robust generalization to novel surveillance indicators. This capability is especially valuable in settings where conventional case counts may be missing

or delayed, but syndromic indicators are available in near real-time.

Across all seven disease forecasting tasks, spanning respiratory, vector-borne, bloodborne, and syndromic targets, Mantis consistently ranked first or second on both point and probabilistic metrics (Table 1). This level of generalization, across diseases, mechanisms, and modalities, demonstrates Mantis’s capacity as a foundation model and the advantages of scaling afforded by simulation data. Rather than relying on domain-specific tuning, Mantis captures structural features of contagion that transfer across contexts, enabling immediate deployment in settings where other models would require retraining, expert tuning, or disease-specific data collection.

Discussion

Mantis demonstrates that accurate forecasting across diverse diseases can be achieved through training on simulated outbreaks, without access to real-world data. By learning from mechanistic simulations, Mantis delivers competitive performance across real-world forecasting tasks spanning multiple transmission modes, outbreak phases, and surveillance systems. These capabilities position Mantis as a practical tool for public health use, especially in low-resource or emerging outbreak settings where data may be limited or delayed. Because Mantis can generate forecasts with only a short initial observation window, it enables early situational awareness when conventional models require longer histories to achieve comparable accuracy. Mantis’s advantage in data-scarce settings stems from its ability to avoid overfitting to sparse initial data. Rather than extrapolating confidently from a handful of observations, Mantis produces appropriately hedged forecasts that reflect the true uncertainty across potential outbreak trajectories, enabling more reliable probabilistic planning even when historical context is minimal.

The implications extend beyond public health. Simulation-supervised learning allows mechanistic models to embed scientific knowledge into neural networks, enabling them to generalize beyond observed data [8, 9]. This paradigm offers a potential solution to a fundamental challenge in epidemiological modeling: real-world disease data are limited by privacy concerns, reporting inconsistencies, and the infrequency of major outbreaks. Simulations, by contrast, can generate unlimited training data spanning diverse scenarios. Whether simulation-based training ultimately proves superior to training on massive real-world datasets—if such data could be assembled—remains an open question. However, given current data availability constraints, the simulation-based approach offers a practical path forward for building general-purpose forecasting systems.

Mantis represents an initial attempt at a foundation model for disease forecasting, and several important questions remain unresolved. First, the optimal neural architecture for this task is unclear. While our hybrid CNN-transformer design performs well, alternative architectures may offer better performance or efficiency trade-offs. Second, the ideal balance between simulation diversity and computational cost requires further investigation. Our training set spans 400 million simulated days, generated continuously until model convergence without repeating data. Using synthetic data like this allows us to avoid the overfitting risks inherent in epoch-based training on fixed datasets. However, whether this scale is necessary or whether comparable performance could be achieved with fewer but more strategically designed simulations remains to be seen.

While Mantis shows broad generalization, several limitations merit consideration. Though we demonstrate generalization beyond the specific regimes directly simulated during training, the model’s performance depends on the diversity and realism of training simulations. Additionally, Mantis inherits any systematic biases present in the underlying mechanistic models used for training. If the simulation framework systematically misrepresents certain disease dynamics—for example, categorically overestimating intervention effects—these biases will propagate to the trained model. Future work should explore approaches to identify and fill critical simulation gaps, and develop methods to validate that training simulations adequately span the space of real-world disease dynamics.

Mantis illustrates a path forward for general-purpose disease forecasting systems that can be quickly deployed without disease-specific tuning. Its out-of-the-box generalization makes it especially well-suited for early outbreak response, rural regions, and low- and middle-income countries—settings where traditional models often fail due to sparse or delayed data. By pairing simulation-based priors with flexible neural architectures, this approach offers a scalable alternative to expert-tuned, disease-specific models. As a first demonstration of simulation-grounded foundation models in infectious disease forecasting, Mantis establishes

both the promise and the open challenges of this paradigm for future decision support systems in global public health.

Methods

A complete description of the methods is given in the Appendix.

Training Mantis on Simulated Outbreaks

Mantis was trained entirely on synthetic outbreaks generated using mechanistic epidemiological models, following the framework developed in [8]. Simulations were based on compartmental disease models with stochastic transitions and heterogeneous parameterizations, using three primary transmission routes: human-to-human respiratory illness models, vectorborne disease models (primarily inspired by arbovirus dynamics), and environmental transmission models (inspired by cholera and other environmentally transmitted pathogens). These models varied in transmission dynamics, disease severity, and intervention strategies to create a broad and diverse training distribution (see Appendix A for details). Each simulation generated daily time series of cases, hospitalizations, and deaths under a wide range of epidemic scenarios. In total, the training dataset included over 400 million days of data spanning thousands of parameter combinations.

Neural Architecture and Training Procedure

Mantis uses a sequence-to-sequence neural network with convolutional and transformer-based components (Appendix B). The model takes an input context window of up to 112 weeks of observed time series and outputs probabilistic forecasts for multiple future targets (e.g., cases, hospitalizations, deaths). Forecasts are trained using a weighted quantile loss. We optimized the neural network using AdamW [20]. No real-world data are used during training.

Evaluation on Real-World Forecasting Tasks

We evaluated Mantis across six diverse real-world infectious disease forecasting scenarios to assess generalization across pathogens, transmission modes, geographic scales, and historical periods (Appendix C). Our evaluation comprised two primary tasks and four additional challenges representing varying degrees of distribution shift from the model’s training data. Together, these datasets encompass over 39 forecasting tasks and more than 150,000 individual forecast evaluations, enabling rigorous assessment of Mantis’s capabilities across diverse epidemiological conditions, spatial resolutions, and outcome types. All Mantis evaluations were conducted in a strict zero-shot setting, with no fine-tuning or retraining on any evaluation data.

Baseline Models

We compared Mantis against two classes of baseline models: operational forecasts from the CDC COVID-19 Forecast Hub and models we re-implemented for evaluation across all diseases. For the CDC COVID-19 Forecast Hub comparison, we used forecasts as originally submitted by modeling teams during the pandemic and, to the best of our ability, evaluated both them and Mantis using the data as it was available at the time of each forecast (i.e., without any backfill or cleaning). This retrospective evaluation means our dataset contains data quality issues (e.g., missing/underreported data) that were present in the original surveillance data and likely affected all models’ performance, including Mantis. These CDC models were retrained or refitted each week to incorporate newly available data, and modeling teams could manually adjust forecasts if their automated systems produced anomalous predictions. Mantis forecasts were not modified in any way. This represents the strongest possible real-world baseline, reflecting operational forecasting practice with expert oversight under realistic data conditions.

For baselines we implemented—including statistical models (exponential smoothing and SARIMA) and deep learning models (LSTM)—we likewise retrained or refitted each model at every forecast point as new data became available. This rolling retraining procedure provides the strongest possible baseline performance for each method. Full baseline model implementation details can be found in Appendix C.

To compute relative MAE and relative WIS, we normalized all forecast errors by the performance of a naïve baseline model. This baseline generates point forecasts by projecting the most recent observed value forward to all future time points. Uncertainty intervals are constructed using the procedure from the COVIDhub-baseline model [2]: we collect all first differences from the historical time series along with their negatives (i.e., $y_t - y_{t-1}$ and $-(y_t - y_{t-1})$ for all past times t). We form a piecewise linear approximation to the empirical cumulative distribution function of these differences, then generate 100,000 Monte Carlo samples by independently drawing sequences of h differences and adding them to the most recent observed value. The resulting distribution is truncated at zero (to prevent negative forecasts) and summarized using quantiles, with the median set equal to the last observed value to eliminate sampling noise. This baseline captures the natural variability in historical changes without making assumptions about future trends, providing a neutral reference point for evaluating forecast skill.

Author Contributions

CD led the study and developed the code and initial draft of the manuscript. CH and AS did the ablation studies and RM developed figure visualizations. CD, MCE, RM, and EM all contributed substantial edits and revisions for the final manuscript.

References

- [1] Emma S McBryde, Michael T Meehan, Oyelola A Adegbeye, Adeshina I Adekunle, Jamie M Caldwell, Anton Pak, Diana P Rojas, Bridget M Williams, and James M Trauer. Role of modelling in covid-19 policy development. *Paediatric Respiratory Reviews*, 35:57–60, Sep 2020.
- [2] Estee Y. Cramer, Evan L. Ray, Velma K. Lopez, Johannes Bracher, Andrea Brennen, Alvaro J. Castro Rivadeneira, Aaron Gerdin, Tilmann Gneiting, Katie H. House, Yuxin Huang, Dasuni Jayawardena, Abdul H. Kanji, Ayush Khandelwal, Khoa Le, Anja Mühlemann, Jarad Niemi, Apurv Shah, Ariane Stark, Yijin Wang, Nutcha Wattanachit, Martha W. Zorn, Youyang Gu, Sansiddh Jain, Nayana Ban nur, Ayush Deva, Mihir Kulkarni, Srujana Merugu, Alpan Raval, Siddhant Shingi, Avtansh Tiwari, Jerome White, Neil F. Abernethy, Spencer Woody, Maytal Dahan, Spencer Fox, Kelly Gaither, Michael Lachmann, Lauren Ancel Meyers, James G. Scott, Mauricio Tec, Ajitesh Srivastava, Glover E. George, Jeffrey C. Cegan, Ian D. Dettwiller, William P. England, Matthew W. Farthing, Robert H. Hunter, Brandon Lafferty, Igor Linkov, Michael L. Mayo, Matthew D. Parno, Michael A. Rowland, Benjamin D. Trump, Yanli Zhang-James, Samuel Chen, Stephen V. Faraone, Jonathan Hess, Christopher P. Morley, Asif Salekin, Dongliang Wang, Sabrina M. Corsetti, Thomas M. Baer, Marisa C. Eisenberg, Karl Falb, Yitao Huang, Emily T. Martin, Ella McCauley, Robert L. Myers, Tom Schwarz, Daniel Sheldon, Graham Casey Gibson, Rose Yu, Liyao Gao, Yian Ma, Dongxia Wu, Xifeng Yan, Xiaoyong Jin, Yu-Xiang Wang, YangQuan Chen, Lihong Guo, Yanting Zhao, Quanquan Gu, Jinghui Chen, Lingxiao Wang, Pan Xu, Weitong Zhang, Difan Zou, Hannah Biegel, Joceline Lega, Steve McConnell, V. P. Nagraj, Stephanie L. Guertin, Christopher Hulme-Lowe, Stephen D. Turner, Yunfeng Shi, Xuegang Ban, Robert Walraven, Qi-Jun Hong, Stanley Kong, Axel van de Walle, James A. Turtle, Michal Ben-Nun, Steven Riley, Pete Riley, Ugur Koayluoglu, David DesRoches, Pedro Forli, Bruce Hamory, Christina Kyriakides, Helen Leis, John Milliken, Michael Moloney, James Morgan, Ninad Nirgudkar, Gokce Ozcan, Noah Pi wonka, Matt Ravi, Chris Schrader, Elizabeth Shakhnovich, Daniel Siegel, Ryan Spatz, Chris Stiefeling, Barrie Wilkinson, Alexander Wong, Sean Cavany, Guido España, Sean Moore, Rachel Oidtman, Alex Perkins, David Kraus, Andrea Kraus, Zhifeng Gao, Jiang Bian, Wei Cao, Juan Lavista Ferres, Chaozhuo Li, Tie-Yan Liu, Xing Xie, Shun Zhang, Shun Zheng, Alessandro Vespiagnani, Matteo Chinazzi, Jessica T. Davis, Kumpeng Mu, Ana Pastore y Piontti, Xinyue Xiong, Andrew Zheng, Jackie Baek, Vivek Farias, Andreea Georgescu, Retsef Levi, Deeksha Sinha, Joshua Wilde, Georgia Perakis, Mohammed Amine Bennouna, David Nze-Ndong, Divya Singhvi, Ioannis Spantidakis, Leann Thayaparan, Asterios Tsiorvas, Arnab Sarker, Ali Jadbabaie, Devavrat Shah, Nicolas Della Penna, Leo A. Celi, Saketh Sundar, Russ Wolfinger, Dave Osthuis, Lauren Castro, Geoffrey Fairchild, Isaac Michaud, Dean Karlen, Matt Kinsey, Luke C. Mullany, Kaitlin Rainwater-Lovett, Lauren Shin, Katharine Tallaksen, Shelby Wilson,

Elizabeth C. Lee, Juan Dent, Kyra H. Grantz, Alison L. Hill, Joshua Kaminsky, Kathryn Kaminsky, Lindsay T. Keegan, Stephen A. Lauer, Joseph C. Lemaitre, Justin Lessler, Hannah R. Meredith, Javier Perez-Saez, Sam Shah, Claire P. Smith, Shaun A. Truelove, Josh Wills, Maximilian Marshall, Lauren Gardner, Kristen Nixon, John C. Burant, Lily Wang, Lei Gao, Zhiling Gu, Myungjin Kim, Xinyi Li, Guannan Wang, Yueying Wang, Shan Yu, Robert C. Reiner, Ryan Barber, Emmanuela Gakidou, Simon I. Hay, Steve Lim, Chris Murray, David Pigott, Heidi L. Gurung, Prasith Baccam, Steven A. Stage, Bradley T. Suchoski, B. Aditya Prakash, Bijaya Adhikari, Jiaming Cui, Alexander Rodríguez, Anika Tabassum, Jiajia Xie, Pinar Keskinocak, John Asplund, Arden Baxter, Buse EYLUL ORUC, Nicoleta Serban, Sercan O. Arik, Mike Dusenberry, Arkady Epshteyn, Elli Kanal, Long T. Le, Chun-Liang Li, Tomas Pfister, Dario Sava, Rajarishi Sinha, Thomas Tsai, Nate Yoder, Jinsung Yoon, Leyou Zhang, Sam Abbott, Nikos I. Bosse, Sebastian Funk, Joel Hellewell, Sophie R. Meakin, Katharine Sherratt, Mingyuan Zhou, Rahi Kalantari, Teresa K. Yamana, Sen Pei, Jeffrey Shaman, Michael L. Li, Dimitris Bertsimas, Omar Skali Lami, Saksham Soni, Hamza Tazi Bouardi, Turgay Ayer, Madeline Adee, Jagpreet Chhatwal, Ozden O. Dalgic, Mary A. Ladd, Benjamin P. Linas, Peter Mueller, Jade Xiao, Yuanjia Wang, Qinxia Wang, Shanghong Xie, Donglin Zeng, Alden Green, Jacob Bien, Logan Brooks, Addison J. Hu, Maria Jahja, Daniel McDonald, Balasubramanian Narasimhan, Collin Politsch, Samyak Rajanala, Aaron Rumack, Noah Simon, Ryan J. Tibshirani, Rob Tibshirani, Valerie Ventura, Larry Wasserman, Eamon B. O'Dea, John M. Drake, Robert Pagano, Quoc T. Tran, Lam Si Tung Ho, Huong Huynh, Jo W. Walker, Rachel B. Slayton, Michael A. Johansson, Matthew Biggerstaff, and Nicholas G. Reich. Evaluation of individual and ensemble probabilistic forecasts of covid-19 mortality in the united states. *Proceedings of the National Academy of Sciences*, 119(15):e2113561119, 2022.

- [3] Alexander Rodriguez, Anika Tabassum, Jiaming Cui, Jiajia Xie, Javen Ho, Pulak Agarwal, Bijaya Adhikari, and Aditya Prakash. Deepcovid: An operational deep learning-driven framework for explainable real-time covid-19 forecasting. In *Proceedings of the AAAI Conference on Artificial Intelligence*, volume 35, 2021.
- [4] Dongxia Wu, Liyao Gao, Xinyue Xiong, Matteo Chinazzi, Alessandro Vespignani, Yi-An Ma, and Rose Yu. Deepgleam: A hybrid mechanistic and deep learning model for covid-19 forecasting, 2021.
- [5] Sebastian Funk, Anton Camacho, Adam J Kucharski, Rachel Lowe, Rosalind M Eggo, and W John Edmunds. Assessing the performance of real-time epidemic forecasts: A case study of ebola in the western area region of sierra leone, 2014–15. *PLOS Computational Biology*, 15(2):e1006785, 2019.
- [6] Nicholas G. Reich et al. Collaborative hubs: Making the most of predictive epidemic modeling. *American Journal of Public Health*, 112(6):839–842, 2022. Epub 2022 Apr 14.
- [7] Michael C. Runge et al. Scenario design for infectious disease projections: Integrating concepts from decision analysis and experimental design. *Epidemics*, 47:100775, 2024. Epub 2024 May 24.
- [8] Carson Dudley, Reiden Magdaleno, Christopher Harding, and Marisa Eisenberg. Simulation as supervision: Mechanistic pretraining for scientific discovery. *arXiv preprint arXiv:2507.08977*, 2025.
- [9] Lijing Wang, Jiangzhuo Chen, and Madhav Marathe. Defsi: Deep learning based epidemic forecasting with synthetic information. In *Proceedings of the AAAI Conference on Artificial Intelligence*, volume 33, 2019.
- [10] University of Michigan. Mi safe start map. Accessed August 15, 2025.
- [11] David C. Farrow, Logan C. Brooks, Aaron Rumack, Ryan J. Tibshirani, and Roni Rosenfeld. Delphi epidata api. <https://github.com/cmu-delphi/delphi-epidata>, 2015. Carnegie Mellon University, Delphi Research Group.
- [12] CDC COVID-19 Response. Weekly united states covid-19 cases and deaths by state - archived. <https://data.cdc.gov/Case-Surveillance/Weekly-United-States-COVID-19-Cases-and-Deaths-by-/pwn4-m3yp>, 2025.

- [13] Willem Van Panhuis, Abigail Cross, and Donald Burke. Counts of dengue without warning signs reported in brazil: 1980–2005 (2.0) [data set]. <https://doi.org/10.25337/T7/ptycho.v2.0/BR.722862003>, 2018. Project Tycho.
- [14] Willem Van Panhuis, Abigail Cross, and Donald Burke. Counts of viral hepatitis type b reported in united states of america: 1951–2007 (2.0) [data set]. <https://doi.org/10.25337/T7/ptycho.v2.0/US.66071002>, 2018. Project Tycho.
- [15] Willem Van Panhuis, Abigail Cross, and Donald Burke. Counts of smallpox reported in united states of america: 1888–1952 (2.0) [data set]. <https://doi.org/10.25337/T7/ptycho.v2.0/US.67924001>, 2018. Project Tycho.
- [16] Willem Van Panhuis, Abigail Cross, and Donald Burke. Counts of scarlet fever reported in united states of america: 1888–1969 (2.0) [data set]. <https://doi.org/10.25337/T7/ptycho.v2.0/US.30242009>, 2018. Project Tycho.
- [17] Johannes Bracher, Evan L. Ray, Tilmann Gneiting, and Nicholas G. Reich. Evaluating epidemic forecasts in an interval format. *PLOS Computational Biology*, 17(2):e1008618, 2021.
- [18] Abdul Fatir Ansari, Lorenzo Stella, Caner Turkmen, Xiyuan Zhang, Pedro Mercado, Huibin Shen, Oleksandr Shchur, Syama Sundar Rangapuram, Sebastian Pineda Arango, Shubham Kapoor, Jasper Zschiegner, Danielle C. Maddix, Hao Wang, Michael W. Mahoney, Kari Torkkola, Andrew Gordon Wilson, Michael Bohlke-Schneider, and Yuyang Wang. Chronos: Transformer-based language models for time-series forecasting, 2024.
- [19] Suprabhath Kalahasti, Benjamin Faucher, Boxuan Wang, Claudio Ascione, Ricardo Carbajal, Maxime Enault, Christophe Vincent Cassis, Titouan Launay, Caroline Guerrisi, Pierre-Yves Boëlle, Federico Baldo, and Eugenio Valdano. Foundation time series models for forecasting and policy evaluation in infectious disease epidemics. *medRxiv*, February 2025. preprint, not peer-reviewed.
- [20] Ilya Loshchilov and Frank Hutter. Decoupled weight decay regularization, 2019.
- [21] Hualei Xin, Yu Li, Peng Wu, Zhili Li, Eric HY Lau, Ying Qin, Liping Wang, Benjamin J Cowling, Tim K Tsang, and Zhongjie Li. Estimating the latent period of coronavirus disease 2019 (covid-19). *Clinical Infectious Diseases*, 74(9):1678–1681, 2022.
- [22] Vincent Ka Chun Yan, Eric Yuk Fai Wan, Xuxiao Ye, Anna Hoi Ying Mok, Francisco Tsz Tsun Lai, Celine Sze Ling Chui, Xue Li, Carlos King Ho Wong, Philip Hei Li, Tiantian Ma, Simon Qin, Chak Sing Lau, Ian Chi Kei Wong, and Esther Wai Yin Chan. Waning effectiveness against covid-19-related hospitalization, severe complications, and mortality with two to three doses of coronavac and bnt162b2: a case–control study. *Emerging Microbes & Infections*, 12:2209201, 2023.

Appendices

A Training Data

Human-to-Human Transmission Simulator

The human-to-human transmission simulator implements a stochastic compartmental model that captures the complex dynamics of respiratory pathogens spreading through direct contact. This simulator generates diverse outbreak scenarios by randomly sampling from wide parameter ranges, producing synthetic epidemics that span the spectrum from influenza-like seasonal patterns to COVID-like pandemic dynamics.

Model Structure

Compartmental Framework The core model follows a flexible SEAIR structure (Susceptible, Exposed, Asymptomatic, Infectious, Recovered) with optional latent periods, asymptomatic transmission, and waning immunity. These structural features are included probabilistically during simulation generation, allowing Mantis to learn from a wide range of outbreak regimes, including both acute and chronic infections, and both simple and complex transmission pathways. For example, in some simulations, all exposed individuals transition directly to the infectious state (i.e., no latent period); in others, asymptomatic infections are excluded, reflecting diseases without subclinical spread.

When fully enabled, the population is divided into five compartments:

$$\frac{dS}{dt} = -\lambda S + \omega R + bN - dS \quad (1)$$

$$\frac{dE}{dt} = \lambda S - \sigma E - dE \quad (2)$$

$$\frac{dA}{dt} = p_a \sigma E - \gamma_a A - dA \quad (3)$$

$$\frac{dI}{dt} = (1 - p_a) \sigma E - \gamma I - dI \quad (4)$$

$$\frac{dR}{dt} = \gamma_a A + \gamma I - \omega R - dR \quad (5)$$

where:

- S : Susceptible individuals
- E : Exposed (latent) individuals
- A : Asymptomatic infectious individuals
- I : Symptomatic infectious individuals
- R : Recovered/immune individuals
- $N = S + E + A + I + R$: Total population

Force of Infection The force of infection λ incorporates contributions from both symptomatic and asymptomatic individuals:

$$\lambda(t) = \beta(t) \cdot s(t) \cdot \left(\frac{I + \alpha A}{N} \right) \cdot m(t) \quad (6)$$

where:

- $\beta(t)$: Time-varying transmission rate (allows for multiple waves)
- $s(t)$: Seasonal forcing factor
- α : Relative transmissibility of asymptomatic individuals
- $m(t)$: Super-spreading multiplier

Model Parameters The model includes the following epidemiological parameters:

- σ : Progression rate from exposed to infectious ($1/\sigma$ = latent period)
- γ : Recovery rate for symptomatic individuals ($1/\gamma$ = infectious period)
- γ_a : Recovery rate for asymptomatic individuals
- ω : Waning immunity rate ($1/\omega$ = duration of immunity)
- p_a : Probability of asymptomatic infection
- b : Birth rate
- d : Death rate

Stochastic Implementation

The continuous-time model is implemented as a discrete-time stochastic process using daily time steps. At each time step t , transitions between compartments are drawn from binomial distributions (equivalent to tau-leaping with large tau, but we found that it improved performance):

$$\text{New exposures} \sim \text{Binomial}(S_t, 1 - e^{-\lambda_t}) \quad (7)$$

$$E \rightarrow I/A \text{ transitions} \sim \text{Binomial}(E_t, 1 - e^{-\sigma}) \quad (8)$$

$$\text{Recoveries from I} \sim \text{Binomial}(I_t, 1 - e^{-\gamma}) \quad (9)$$

$$\text{Recoveries from A} \sim \text{Binomial}(A_t, 1 - e^{-\gamma_a}) \quad (10)$$

$$\text{Waning immunity} \sim \text{Binomial}(R_t, 1 - e^{-\omega}) \quad (11)$$

Among newly infectious individuals, the split between asymptomatic and symptomatic follows:

$$\text{New asymptomatic} \sim \text{Binomial}(\text{New infectious}, p_a) \quad (12)$$

Multi-Wave Dynamics

To capture realistic outbreak patterns with multiple waves, the transmission rate $\beta(t)$ is implemented as a piecewise constant function:

$$\beta(t) = \beta_i \quad \text{for } t \in [t_{i-1}, t_i) \quad (13)$$

where t_0, t_1, \dots, t_k are randomly chosen wave change points and $\beta_1, \beta_2, \dots, \beta_k$ are independently sampled transmission rates. The number of wave changes is drawn from a discrete uniform distribution, and change points are sampled uniformly within the simulation period.

Seasonal Forcing

Seasonal transmission patterns are modeled using multiple harmonic components:

$$s(t) = 1 + \sum_{j=1}^{n_h} A_j \cos \left(\frac{2\pi(t - \phi_j + \delta_y)}{P_j} \right) + \epsilon_t \quad (14)$$

where:

- n_h : Number of harmonic components (1-4)
- A_j : Amplitude of harmonic j

- P_j : Period of harmonic j (365.0, 182.5, or 91.25 days)
- ϕ_j : Phase offset for harmonic j
- δ_y : Annual peak jitter, sampled independently each year to slightly shift seasonal peaks and avoid perfectly periodic recurrence
- ϵ_t : Daily multiplicative noise $\sim \mathcal{N}(1, 0.05^2)$

Super-Spreading Events

Super-spreading is modeled through a stochastic multiplier applied to the force of infection. At each time step, a subset of infectious individuals becomes super-spreaders with probability p_{ss} . The transmission enhancement follows a Gamma distribution:

$$m(t) = \left(1 - \frac{n_{ss}}{n_I}\right) + \frac{n_{ss}}{n_I} \cdot M \quad (15)$$

where $n_{ss} \sim \text{Binomial}(n_I, p_{ss})$ and $M \sim \text{Gamma}(k_{ss}, \theta_{ss})$.

Intervention Policies

The simulator includes an optional universal intervention policy that modulates transmission based on case thresholds. The policy operates through a contact reduction factor applied to $\beta(t)$:

$$\beta_{eff}(t) = \beta(t) \cdot r_{contact}(t) \quad (16)$$

where $r_{contact}(t) \in [0.2, 1.0]$ represents the intervention strength. The policy activates when daily cases exceed an on-threshold and deactivates after cases remain below an off-threshold for a specified duration.

Endemic Dynamics

For simulations with endemic circulation, demographic processes are included:

$$\text{Births} \sim \text{Poisson}(b \cdot N) \quad (17)$$

$$\text{Deaths} \sim \text{Binomial}(X, \min(d, 1)) \quad \forall X \in \{S, E, A, I, R\} \quad (18)$$

$$\text{Importations} \sim \text{Poisson}(\iota) \quad (19)$$

New births enter the susceptible compartment, deaths occur proportionally across all compartments, and imported cases enter the exposed or infectious compartment.

Observation Model

True epidemic dynamics are converted to observed case counts through a comprehensive noise injection pipeline that simulates real-world surveillance artifacts:

Multiplicative Noise Base case counts are perturbed with log-normal noise:

$$\hat{C}_t = C_t \cdot \epsilon_t, \quad \epsilon_t \sim \text{LogNormal}(0, \sigma_{mult}^2) \quad (20)$$

Underreporting Reporting rates evolve logically over time:

$$r_t = r_0 + (r_\infty - r_0) \cdot \frac{1}{1 + e^{-k(t-t_{mid})}} \quad (21)$$

Reported cases follow: $\tilde{C}_t \sim \text{Binomial}(\hat{C}_t, r_t)$

Reporting Delays Cases are distributed across future days using inverse-weighted delay distributions:

$$P(\text{delay} = d) \propto \frac{\alpha}{d+1}, \quad d \in [0, D_{max}] \quad (22)$$

Day-of-Week Effects Reporting varies by weekday with multiplicative factors:

$$\tilde{C}'_t = \tilde{C}_t \cdot w(\text{day-of-week}(t)) \quad (23)$$

where $w(\cdot)$ ranges from 0.4 (weekend) to 1.2 (Tuesday).

Hospitalization and Death Generation

Secondary outcomes (hospitalizations and deaths) are derived from symptomatic cases using time-varying probabilities and delay distributions. For each wave segment i , hospitalization and death probabilities ($p_{h,i}$ and $p_{d,i}$) are independently sampled.

Hospitalization Process

$$H_t = \sum_{\tau=0}^t \text{Binomial}(I_{\tau}, p_{h, \text{wave}(\tau)}) \cdot f_h(t - \tau) \quad (24)$$

$$f_h(d) \sim \text{Gamma}(k_h, \theta_h) \quad (25)$$

Death Process Deaths occur among hospitalized individuals with additional delays:

$$D_t = \sum_{\tau=0}^t \sum_{s=0}^{\tau} \text{Binomial}(H_{\tau,s}, p_{d, \text{wave}(s)}) \cdot f_d(t - \tau) \quad (26)$$

$$f_d(d) \sim \text{Gamma}(k_d, \theta_d) \quad (27)$$

where $H_{\tau,s}$ represents hospitalizations on day τ originating from infections on day s .

Parameter Ranges

Table 2 summarizes all parameters and their sampling distributions used in the human-to-human transmission simulator. Parameters were chosen to be broadly consistent with respiratory pathogens.

Table 2: Human-to-Human Transmission Simulator Parameters

Parameter	Symbol	Range/Distribution	Units
Population and Simulation			
Population size	N	Log-uniform[50,000, 40,000,000]	individuals
Simulation days	T	2,000	days
Core Transmission Parameters			
Base transmission rate	β	Uniform[0.2, 0.235]	day^{-1}
Recovery rate	γ	Uniform[0.1, 0.33]	day^{-1}
Latent progression rate	σ	Uniform[0.2, 0.4] [21]	day^{-1}
Waning immunity rate	ω	Uniform[0.001, 0.0075] [22]	day^{-1}
Asymptomatic Dynamics			
Asymptomatic probability	p_a	Beta(3, 7)	proportion
Asymp. transmissibility	α	Beta(2, 5)	proportion

Continued on next page

Table 2 – continued from previous page

Parameter	Symbol	Range/Distribution	Units
Has asymptomatic compartment	-	Bernoulli(0.5)	boolean
Model Structure Options			
Has latent period	-	Bernoulli(0.7)	boolean
Has waning immunity	-	Bernoulli(0.9)	boolean
Multi-Wave Dynamics			
Multiple waves enabled	-	Configurable (default: True)	boolean
Number of wave changes	-	Uniform[0, 4]	count
Wave change days	-	Uniform[50, 1800]	days
Super-Spreading			
Super-spreader probability	p_{ss}	Uniform[0.0005, 0.02]	proportion
Multiplier shape	k_{ss}	4.0	-
Multiplier scale	θ_{ss}	1.5	-
Seasonality			
Use seasonality	-	Bernoulli(0.8)	boolean
Number of harmonics	n_h	Uniform[1, 4]	count
Harmonic amplitude	A_j	Base \times Uniform[0.3, 1.0]	proportion
Base amplitude	-	Uniform[0.1, 0.5]	proportion
Phase offset	ϕ_j	Uniform[0, 365] + Uniform[-60, 60]	days
Possible periods	P_j	Choice[365.0, 182.5, 91.25]	days
Daily noise std	σ_ϵ	0.05	proportion
Annual peak jitter	δ_y	Uniform[-30, 30]	days
Endemic Demographics			
Enable endemic	-	Bernoulli(0.8)	boolean
Birth rate	b	Uniform[0.00002, 0.00012]	day $^{-1}$
Death rate factor	-	Uniform[0.8, 1.3]	proportion
Importation rate	ι	Exp(Uniform[ln(0.01), ln(0.5)])	day $^{-1}$
Intervention Policy			
Enable intervention	-	Bernoulli(0.25)	boolean
On threshold	-	$N \times$ Uniform[1e-5, 1e-3]	cases/day
Off threshold	-	On threshold \times Uniform[0, 1]	cases/day
Contact reduction	$r_{contact}$	Uniform[0.2, 0.6]	proportion
Trigger delay	-	Uniform[0, 21]	days
Minimum duration	-	Uniform[14, 35]	days
Maximum duration	-	Choice[None, Uniform[60, 120]]	days
Consecutive off days	-	Uniform[1, 50]	days
Observation Noise			
Multiplicative noise std	σ_{mult}	0.1	log-scale
Overdispersion parameter	r	1200	-
Reporting Effects			
Apply reporting rate	-	Bernoulli(0.8)	boolean
Initial reporting rate	r_0	Uniform[0.05, 0.4]	proportion
Final reporting rate	r_∞	Uniform[0.25, 0.85]	proportion
Days to max testing	-	Uniform[30, 365]	days
Logistic steepness	k	Uniform[4, 8]	-

Continued on next page

Table 2 – continued from previous page

Parameter	Symbol	Range/Distribution	Units
Apply weekday effects	-	Bernoulli(0.8)	boolean
Monday factor	-	Normal(1.2, 0.15)	proportion
Tue-Thu factor	-	Normal(1.0, 0.1)	proportion
Friday factor	-	Normal(0.9, 0.12)	proportion
Saturday factor	-	Normal(0.6, 0.2)	proportion
Sunday factor	-	Normal(0.4, 0.2)	proportion
Apply lab noise	-	Bernoulli(0.8)	boolean
Lab batch size	-	Poisson(100)	samples
Bad batch rate	-	0.005	proportion
Bad batch accuracy	-	Uniform[0.7, 0.85]	proportion
Apply delays	-	Bernoulli(0.8)	boolean
Initial max delay	-	Uniform[7, 21]	days
Final max delay	-	Uniform[2, 7]	days
Initial alpha	α_0	1.0	-
Final alpha	α_∞	4.0	-
Hospitalization & Death			
Hospitalization probability	$p_{h,i}$	Uniform[0.02, 0.15] per wave	proportion
Death probability (of hosp.)	$p_{d,i}$	Uniform[0.05, 0.3] per wave	proportion
Hosp. delay shape	k_h	Uniform[2.0, 4.0]	-
Hosp. delay scale	θ_h	Uniform[1.0, 3.0]	days
Death delay shape	k_d	Uniform[1.5, 2.5]	-
Death delay scale	θ_d	Uniform[4.5, 8.5]	days

This comprehensive parameter space enables the generation of diverse outbreak scenarios spanning different pathogen characteristics, population contexts, surveillance qualities, and intervention regimes. Each simulation run samples independently from these distributions, creating a rich training corpus that captures the full spectrum of human-to-human transmission dynamics.

Vector-Borne Transmission Simulator

The vector-borne transmission simulator implements a coupled host-vector compartmental model that captures the complex dynamics of diseases transmitted through arthropod vectors, such as dengue, Zika, chikungunya, and malaria. This simulator models the epidemiological dynamics within both human and vector populations, incorporating realistic vector ecology, seasonal patterns, and intervention strategies.

Model Structure

Coupled Host-Vector Framework The model consists of two interacting population systems: humans and vectors (typically mosquitoes). The human population follows a SEAIR structure similar to the human-to-human model, while vectors follow a simpler SEI structure without recovery (as infected vectors typically remain infectious for life).

Human Population Dynamics The human compartments evolve according to:

$$\frac{dS_h}{dt} = -\lambda_h S_h + \omega R_h + b_h N_h - d_h S_h \quad (28)$$

$$\frac{dE_h}{dt} = \lambda_h S_h - \sigma_h E_h - d_h E_h \quad (29)$$

$$\frac{dA_h}{dt} = p_a \sigma_h E_h - \gamma_a A_h - d_h A_h \quad (30)$$

$$\frac{dI_h}{dt} = (1 - p_a) \sigma_h E_h - \gamma I_h - d_h I_h \quad (31)$$

$$\frac{dR_h}{dt} = \gamma_a A_h + \gamma I_h - \omega R_h - d_h R_h \quad (32)$$

Vector Population Dynamics The vector compartments evolve according to:

$$\frac{dS_v}{dt} = \mu_v N_v - \lambda_v S_v - \mu_v S_v \quad (33)$$

$$\frac{dE_v}{dt} = \lambda_v S_v - \sigma_v E_v - \mu_v E_v \quad (34)$$

$$\frac{dI_v}{dt} = \sigma_v E_v - \mu_v I_v \quad (35)$$

where $N_v = S_v + E_v + I_v$ is the total vector population.

Force of Infection The transmission between humans and vectors occurs through biting interactions. The force of infection for humans (from infected vectors) is:

$$\lambda_h(t) = a \cdot b_h \cdot \frac{I_v}{N_v} \cdot \beta(t) \cdot s(t) \cdot f_{intervention}(t) \quad (36)$$

The force of infection for vectors (from infected humans) is:

$$\lambda_v(t) = a \cdot b_v \cdot \frac{I_h + \alpha A_h}{N_h} \cdot \beta(t) \cdot s(t) \cdot f_{intervention}(t) \quad (37)$$

where:

- a : Biting rate (bites per vector per day)
- b_h : Probability of transmission from vector to human per bite
- b_v : Probability of transmission from human to vector per bite
- $\beta(t)$: Time-varying transmission scaling factor
- $s(t)$: Seasonal forcing function
- $f_{intervention}(t)$: Intervention effectiveness factor
- α : Relative transmissibility of asymptomatic humans

Stochastic Implementation

The continuous-time model is implemented as a discrete-time stochastic process. At each time step t , transitions are drawn from binomial distributions:

Human Transitions

$$\text{New human exposures} \sim \text{Binomial}(S_h(t), 1 - e^{-\lambda_h(t)}) \quad (38)$$

$$E_h \rightarrow I_h / A_h \sim \text{Binomial}(E_h(t), 1 - e^{-\sigma_h}) \quad (39)$$

$$\text{Human recoveries from } I \sim \text{Binomial}(I_h(t), 1 - e^{-\gamma}) \quad (40)$$

$$\text{Human recoveries from } A \sim \text{Binomial}(A_h(t), 1 - e^{-\gamma_a}) \quad (41)$$

$$\text{Waning immunity} \sim \text{Binomial}(R_h(t), 1 - e^{-\omega}) \quad (42)$$

Vector Transitions

$$\text{New vector exposures} \sim \text{Binomial}(S_v(t), 1 - e^{-\lambda_v(t)}) \quad (43)$$

$$E_v \rightarrow I_v \sim \text{Binomial}(E_v(t), 1 - e^{-\sigma_v}) \quad (44)$$

$$\text{Vector deaths from } S \sim \text{Binomial}(S_v(t), \mu_v) \quad (45)$$

$$\text{Vector deaths from } E \sim \text{Binomial}(E_v(t), \mu_v) \quad (46)$$

$$\text{Vector deaths from } I \sim \text{Binomial}(I_v(t), \mu_v) \quad (47)$$

$$\text{New vector births} \sim \text{Poisson}(\mu_v N_v(t)) \quad (48)$$

Vector Population Dynamics

Vector populations exhibit distinct ecological patterns compared to human populations:

Mortality and Reproduction Vectors have high mortality rates (μ_v) with typical lifespans of 10-30 days. To maintain population equilibrium, new vectors are born at rate $\mu_v N_v$, entering the susceptible class.

Seasonal Patterns Vector abundance and activity are strongly seasonal, captured through enhanced seasonal forcing:

$$s(t) = 1.2 + \sum_{j=1}^{n_h} A_j \cos\left(\frac{2\pi(t - \phi_j + \delta_y)}{P_j}\right) + \epsilon_t \quad (49)$$

The baseline value (1.2) and amplitude ranges ($A_j \in [0.5, 1.25]$) are increased compared to human-to-human transmission to reflect the stronger seasonal dependence of vector-borne diseases.

Multi-Wave Dynamics

Similar to the human-to-human simulator, vector-borne outbreaks can exhibit multiple waves through time-varying transmission scaling:

$$\beta(t) = \beta_i \quad \text{for } t \in [t_{i-1}, t_i) \quad (50)$$

However, for vector-borne diseases, wave changes often reflect environmental conditions affecting vector populations (rainfall, temperature) or intervention campaigns rather than behavioral changes.

Intervention Modeling

Vector control interventions are modeled through the reduction factor $f_{intervention}(t)$ applied to both λ_h and λ_v . Common interventions include:

- **Vector control:** Reduces vector population or biting rates
- **Larvicide applications:** Affects vector reproduction
- **Personal protection:** Reduces effective contact rates

- **Environmental management:** Modifies vector habitat suitability

The intervention policy triggers based on human case thresholds but affects the vector reduction parameter:

$$f_{intervention}(t) = \begin{cases} f_{vector} & \text{if intervention active} \\ 1.0 & \text{otherwise} \end{cases} \quad (51)$$

where $f_{vector} \in [0.2, 0.6]$ represents the effectiveness of vector control measures.

Initialization Strategy

Human Population Initial conditions allow for pre-existing immunity in the human population:

$$\text{Immune fraction} \sim \text{Uniform}(0, 0.7) \quad (52)$$

$$\text{Initial infections} \sim \text{NegativeBinomial}(n = \max(1, N_h \times 5 \times 10^{-6}), p = 0.5) \quad (53)$$

Vector Population Vector populations start with a small fraction exposed/infected:

$$N_v = N_h \times \text{Uniform}(2.0, 10.0) \quad (54)$$

$$\text{Initial vector exposures} \sim \text{NegativeBinomial}(n = \max(1, N_v \times 10^{-4}), p = 0.3) \quad (55)$$

The higher initial prevalence in vectors reflects their role as reservoirs and their shorter generation times.

Parameter Ranges

Table 3 summarizes all parameters specific to the vector-borne transmission simulator.

Table 3: Vector-Borne Transmission Simulator Parameters

Parameter	Symbol	Range/Distribution	Units
Human Population (Shared with H2H)			
Population size	N_h	Log-uniform[50,000, 40,000,000]	individuals
Base transmission scaling	β	Uniform[0.5, 0.7]	-
Recovery rate	γ	Uniform[0.1, 0.33]	day^{-1}
Latent progression rate	σ_h	Uniform[0.2, 0.4] [21]	day^{-1}
Waning immunity rate	ω	Uniform[0.003, 0.02] [22]	day^{-1}
Asymptomatic probability	p_a	Beta(3, 7)	proportion
Asymp. transmissibility	α	Beta(2, 5)	proportion
Vector Population Dynamics			
Vector population size	N_v	$N_h \times \text{Uniform}[2.0, 10.0]$	individuals
Vector mortality rate	μ_v	Uniform[0.03, 0.10]	day^{-1}
Vector latent progression	σ_v	Uniform[0.15, 0.30]	day^{-1}
Vector lifespan	$1/\mu_v$	Uniform[10, 33]	days
Extrinsic incubation	$1/\sigma_v$	Uniform[3.3, 6.7]	days
Transmission Parameters			
Biting rate	a	Uniform[0.40, 0.80]	bites/vector/day
Vector→human transmission	b_h	Uniform[0.35, 0.75]	probability

Continued on next page

Table 3 – continued from previous page

Parameter	Symbol	Range/Distribution	Units
Human→vector transmission	b_v	Uniform[0.35, 0.75]	probability
Model Structure Options			
Has latent period	-	Bernoulli(0.7)	boolean
Has asymptomatic compartment	-	Bernoulli(0.5)	boolean
Has waning immunity	-	Bernoulli(1.0)	boolean
Enhanced Seasonality			
Use seasonality	-	Bernoulli(0.8)	boolean
Base seasonal value	-	1.2	-
Harmonic amplitude range	A_j	Base \times Uniform[0.3, 1.0]	proportion
Base amplitude	-	Uniform[0.5, 1.25]	proportion
Number of harmonics	n_h	Uniform[1, 4]	count
Multi-Wave Dynamics			
Multiple waves enabled	-	Configurable (default: True)	boolean
Number of wave changes	-	Uniform[0, 4]	count
Wave change timing	-	Uniform[50, 1800]	days
Vector Control Interventions			
Enable intervention	-	Bernoulli(0.25)	boolean
On threshold	-	$N_h \times$ Uniform[1e-5, 1e-3]	cases/day
Off threshold	-	On threshold \times Uniform[0, 1]	cases/day
Vector reduction	f_{vector}	Uniform[0.2, 0.6]	proportion
Trigger delay	-	Uniform[0, 21]	days
Minimum duration	-	Uniform[14, 35]	days
Maximum duration	-	Choice[None, Uniform[60, 120]]	days
Consecutive off days	-	Uniform[1, 50]	days
Initialization Parameters			
Human immune fraction	-	Uniform[0.0, 0.7]	proportion
Initial human infections	-	NegBin($n = \max(1, N_h \times 5e^{-6})$, $p = 0.5$)	count
Vector:human ratio	-	Uniform[2.0, 10.0]	ratio
Initial vector exposures	-	NegBin($n = \max(1, N_v \times 1e^{-4})$, $p = 0.3$)	count
Observation & Outcomes (Shared)			
Hospitalization probability	p_h	Uniform[0.05, 0.20]	proportion
Death probability (of hosp.)	p_d	Uniform[0.10, 0.40]	proportion
Hosp. delay shape	k_h	Uniform[2.0, 4.0]	-
Hosp. delay scale	θ_h	Uniform[1.0, 3.0]	days
Death delay shape	k_d	Uniform[1.5, 2.5]	-
Death delay scale	θ_d	Uniform[2.0, 5.0]	days
Noise & Reporting (Identical to H2H)			
Multiplicative noise std	σ_{mult}	0.1	log-scale
Reporting effects	-	Same as Table 2	various

Continued on next page

Table 3 – continued from previous page

Parameter	Symbol	Range/Distribution	Units
Day-of-week effects	-	Same as Table 2	various
Lab noise parameters	-	Same as Table 2	various
Delay distributions	-	Same as Table 2	various

Key Differences from Human-to-Human Transmission

The vector-borne simulator incorporates several critical differences that distinguish it from direct human-to-human transmission:

Dual Population Dynamics Unlike human-to-human models, vector-borne diseases require explicit modeling of vector population dynamics, including birth, death, and infection processes within the arthropod population.

Transmission Pathway Transmission requires a two-step process (human \rightarrow vector \rightarrow human) rather than direct contact, fundamentally altering the epidemic dynamics and introducing additional delay and complexity.

Environmental Sensitivity Vector-borne diseases exhibit stronger seasonal patterns due to vector ecology dependence on temperature, rainfall, and other environmental factors, reflected in enhanced seasonal forcing parameters.

Vector-Specific Interventions Control strategies focus on vector population reduction rather than behavioral modifications, affecting both λ_h and λ_v through environmental rather than social mechanisms.

Basic Reproduction Number R_0 calculations must account for the round-trip transmission cycle and vector population dynamics, resulting in a more complex formulation that depends on vector:human ratios and vector survival probabilities.

This comprehensive parameter space enables realistic simulation of diverse vector-borne disease scenarios, capturing the full spectrum of arthropod-transmitted pathogen dynamics across different ecological contexts, intervention strategies, and surveillance systems.

Environmental Transmission Simulator

The environmental transmission simulator implements a hybrid compartmental model that captures diseases transmitted through both direct human-to-human contact and indirect environmental pathways via contaminated water sources. This simulator models pathogens such as cholera, typhoid, hepatitis A, and norovirus, which exhibit complex transmission dynamics involving multiple routes of exposure and environmental persistence.

Model Structure

Dual-Route Transmission Framework The waterborne model extends the basic SEAIR structure to include an additional environmental compartment representing pathogen concentration in water. The model simultaneously tracks both direct contact transmission (similar to respiratory diseases) and indirect transmission through contaminated water or environmental sources.

Human Population Dynamics The human compartments follow the same structure as the human-to-human model:

$$\frac{dS}{dt} = -\lambda_h S + \omega R + bN - dS \quad (56)$$

$$\frac{dE}{dt} = \lambda_h S - \sigma E - dE \quad (57)$$

$$\frac{dA}{dt} = p_a \sigma E - \gamma_a A - dA \quad (58)$$

$$\frac{dI}{dt} = (1 - p_a) \sigma E - \gamma I - dI \quad (59)$$

$$\frac{dR}{dt} = \gamma_a A + \gamma I - \omega R - dR \quad (60)$$

Environmental Pathogen Dynamics The environmental water compartment evolves according to:

$$\frac{dW}{dt} = \eta_I I + \eta_A A - \mu_w W \quad (61)$$

where:

- W : Pathogen concentration in water sources
- η_I : Contamination rate from symptomatic individuals
- η_A : Contamination rate from asymptomatic individuals
- μ_w : Pathogen decay/removal rate in water

Composite Force of Infection The total force of infection combines both transmission routes:

$$\lambda_h(t) = \lambda_{contact}(t) + \lambda_{water}(t) \quad (62)$$

where:

$$\lambda_{contact}(t) = \beta(t) \cdot s(t) \cdot \frac{I + \alpha A}{N} \cdot f_{contact}(t) \quad (63)$$

$$\lambda_{water}(t) = \delta(t) \cdot s(t) \cdot W \cdot f_{water}(t) \quad (64)$$

The parameters are:

- $\beta(t)$: Time-varying contact transmission rate
- $\delta(t)$: Time-varying waterborne transmission rate
- $s(t)$: Seasonal forcing factor (affects both routes)
- $f_{contact}(t), f_{water}(t)$: Intervention effectiveness factors
- α : Relative transmissibility of asymptomatic individuals

Multi-Route Wave Dynamics

Waterborne diseases can exhibit complex temporal patterns due to independent variation in both transmission routes. The model implements time-varying transmission coefficients for both pathways:

$$\beta(t) = \beta_i \quad \text{for } t \in [t_{i-1}, t_i) \quad (65)$$

$$\delta(t) = \delta_i \quad \text{for } t \in [t_{i-1}, t_i) \quad (66)$$

Wave changes can reflect:

- **Contact route changes:** Behavioral modifications, crowding patterns, hygiene practices
- **Water route changes:** Infrastructure failures, seasonal water quality, sanitation disruptions
- **Coordinated changes:** Public health interventions affecting both routes simultaneously

Environmental Contamination Process

Contamination Sources Both symptomatic and asymptomatic individuals contribute to environmental contamination:

$$\text{Daily contamination} = \eta_I \cdot I + \eta_A \cdot A \cdot \alpha_{env} \quad (67)$$

where η_I and η_A represent base contamination rates, and α_{env} is the relative environmental shedding from asymptomatic individuals.

Pathogen Persistence and Decay Environmental pathogens undergo exponential decay:

$$\frac{dW}{dt} \Big|_{\text{decay}} = -\mu_w W \quad (68)$$

The decay rate μ_w encompasses multiple removal mechanisms:

- Natural pathogen die-off
- Water treatment processes
- Dilution effects
- UV radiation and temperature effects

Stochastic Implementation

The continuous-time model is implemented stochastically with daily time steps:

Human Transmission Events

$$\text{Contact exposures} \sim \text{Binomial}(S(t), 1 - e^{-\lambda_{contact}(t)}) \quad (69)$$

$$\text{Water exposures} \sim \text{Binomial}(S(t), 1 - e^{-\lambda_{water}(t)}) \quad (70)$$

$$\text{Total new exposures} = \text{Contact exposures} + \text{Water exposures} \quad (71)$$

Note: In the stochastic implementation, total exposures are calculated as:

$$\text{Total exposures} \sim \text{Binomial}(S(t), 1 - e^{-(\lambda_{contact}(t) + \lambda_{water}(t))}) \quad (72)$$

Environmental Process Updates

$$\text{New contamination} = \eta_I \cdot I(t) + \eta_A \cdot A(t) \cdot \alpha_{env} \quad (73)$$

$$\text{Pathogen decay} = \mu_w \cdot W(t) \quad (74)$$

$$W(t+1) = \max(0, W(t) + \text{New contamination} - \text{Pathogen decay}) \quad (75)$$

Compartment Transitions Human compartment transitions follow the same binomial processes as the human-to-human model:

$$E \rightarrow I/A \sim \text{Binomial}(E(t), 1 - e^{-\sigma}) \quad (76)$$

$$\text{Recovery from I} \sim \text{Binomial}(I(t), 1 - e^{-\gamma}) \quad (77)$$

$$\text{Recovery from A} \sim \text{Binomial}(A(t), 1 - e^{-\gamma_a}) \quad (78)$$

$$\text{Waning immunity} \sim \text{Binomial}(R(t), 1 - e^{-\omega}) \quad (79)$$

Enhanced Seasonality

Waterborne diseases exhibit strong seasonal patterns due to environmental factors affecting both transmission routes and pathogen survival:

$$s(t) = 1.0 + \sum_{j=1}^{n_h} A_j \cos \left(\frac{2\pi(t - \phi_j + \delta_y)}{P_j} \right) + \epsilon_t \quad (80)$$

Seasonal Factors Seasonality in waterborne diseases reflects:

- **Rainfall patterns:** Affecting water contamination and treatment efficacy
- **Temperature effects:** Influencing pathogen survival in water
- **Flooding events:** Disrupting sanitation infrastructure
- **Social patterns:** Seasonal migration, gatherings, and water usage

Enhanced Amplitude Range Waterborne diseases show stronger seasonal variation with amplitude parameters:

$$A_j \in [0.6, 1.5] \text{ (compared to } [0.1, 0.5] \text{ for human-to-human)} \quad (81)$$

Dual-Route Intervention Modeling

Interventions can target either or both transmission routes with different effectiveness:

$$\lambda_{contact,eff}(t) = \lambda_{contact}(t) \cdot f_{contact}(t) \quad (82)$$

$$\lambda_{water,eff}(t) = \lambda_{water}(t) \cdot f_{water}(t) \quad (83)$$

Contact Route Interventions Similar to human-to-human diseases:

- Social distancing measures
- Hygiene promotion
- Isolation of cases

Water Route Interventions Specific to environmental transmission:

- Water treatment and chlorination
- Sanitation infrastructure improvements
- Safe water distribution
- Waste management systems

Intervention Policy The universal intervention policy can independently affect both routes:

$$f_{contact}(t) \in [0.2, 0.6] \text{ when intervention active} \quad (84)$$

$$f_{water}(t) \in [0.3, 0.7] \text{ when intervention active} \quad (85)$$

Super-Spreading Events

Super-spreading affects only the contact transmission route, as waterborne transmission is mediated by environmental persistence rather than individual variation:

$$\lambda_{contact,ss}(t) = \lambda_{contact}(t) \cdot m_{ss}(t) \quad (86)$$

where $m_{ss}(t)$ follows the same gamma-distributed multiplier as in human-to-human transmission.

Initialization Strategy

Human Population Initial conditions allow for higher pre-existing immunity due to endemic circulation:

$$\text{Immune fraction} \sim \text{Beta}(10, 3.5) \text{ (higher mean than H2H)} \quad (87)$$

$$\text{Initial infections} \sim \text{NegativeBinomial}(n = N_h \times 10^{-6}, p = 0.5) \quad (88)$$

Environmental Pathogen Load The water compartment initializes at zero, building up through contamination from initial infections:

$$W(0) = 0 \quad (89)$$

Parameter Ranges

Table 4 summarizes all parameters specific to the waterborne transmission simulator.

Table 4: Waterborne Transmission Simulator Parameters

Parameter	Symbol	Range/Distribution	Units
Human Population (Shared)			
Population size	N	Log-uniform[50,000, 40,000,000]	individuals
Recovery rate	γ	Uniform[0.1, 0.33]	day^{-1}
Latent progression rate	σ	Uniform[0.2, 0.4]	day^{-1}
Waning immunity rate	ω	Uniform[0.001, 0.01]	day^{-1}
Asymptomatic probability	p_a	Beta(3, 7)	proportion
Asymp. transmissibility	α	Beta(2, 5)	proportion
Dual-Route Transmission			
Contact transmission rate	β	Uniform[0.0, 0.05]	day^{-1}
Water transmission rate	δ	Uniform[0.0005, 0.01]	day^{-1}
Water contamination rate	η	Uniform[0.001, 0.01]	day^{-1}
Pathogen decay rate	μ_w	Uniform[0.05, 0.3]	day^{-1}
Pathogen half-life	$\ln(2)/\mu_w$	Uniform[2.3, 13.9]	days
Model Structure Options			
Has latent period	-	Bernoulli(0.7)	boolean
Has asymptomatic compartment	-	Bernoulli(0.6)	boolean
Has waning immunity	-	Bernoulli(0.9)	boolean
Multi-Wave Dynamics			

Continued on next page

Table 4 – continued from previous page

Parameter	Symbol	Range/Distribution	Units
Multiple waves enabled	-	Configurable (default: True)	boolean
Number of wave changes	-	Uniform[0, 7]	count
Wave change timing	-	Uniform[50, 1800]	days
Contact wave segments	-	Wave count + 1	count
Water wave segments	-	Wave count + 1	count
Enhanced Seasonality			
Use seasonality	-	Bernoulli(0.9)	boolean
Number of harmonics	n_h	Uniform[1, 4]	count
Base amplitude	-	Uniform[0.6, 1.5]	proportion
Harmonic amplitude	A_j	Base \times Uniform[0.3, 1.0]	proportion
Phase offset	ϕ_j	Uniform[0, 365] + Uniform[-60, 60]	days
Possible periods	P_j	Choice[365.0, 182.5, 91.25]	days
Daily noise std	σ_ϵ	0.05	proportion
Annual peak jitter	δ_y	Uniform[-30, 30]	days
Dual-Route Interventions			
Enable intervention	-	Bernoulli(0.25)	boolean
On threshold	-	$N \times$ Uniform[1e-5, 1e-3]	cases/day
Off threshold	-	On threshold \times Uniform[0, 1]	cases/day
Contact reduction	$f_{contact}$	Uniform[0.2, 0.6]	proportion
Water reduction	f_{water}	Uniform[0.3, 0.7]	proportion
Trigger delay	-	Uniform[0, 21]	days
Minimum duration	-	Uniform[14, 35]	days
Maximum duration	-	Choice[None, Uniform[60, 120]]	days
Consecutive off days	-	Uniform[1, 50]	days
Super-Spreading (Contact Only)			
Super-spreader probability	p_{ss}	Uniform[0.0002, 0.02]	proportion
Multiplier shape	k_{ss}	4.0	-
Multiplier scale	θ_{ss}	1.5	-
Endemic Demographics			
Enable endemic	-	Bernoulli(0.8)	boolean
Birth rate	b	Uniform[0.00002, 0.00012]	day ⁻¹
Death rate factor	-	Uniform[0.8, 1.3]	proportion
Importation rate	ι	Exp(Uniform[ln(0.01), ln(0.5)])	day ⁻¹
Initialization Parameters			
Novel outbreak probability	-	0.0 (always endemic)	proportion
Immune fraction (if endemic)	-	Beta(10, 3.5)	proportion
Initial infections	-	NegBin($n = N \times 10^{-6}$, $p = 0.5$)	count
Initial water pathogen load	$W(0)$	0.0	concentration
Observation & Outcomes			
Hospitalization probability	p_h	Uniform[0.02, 0.15]	proportion
Death probability (of hosp.)	p_d	Uniform[0.05, 0.3]	proportion
Hosp. delay shape	k_h	Uniform[2.0, 4.0]	-

Continued on next page

Table 4 – continued from previous page

Parameter	Symbol	Range/Distribution	Units
Hosp. delay scale	θ_h	Uniform[1.0, 3.0]	days
Death delay shape	k_d	Uniform[1.5, 2.5]	-
Death delay scale	θ_d	Uniform[2.0, 5.0]	days
Noise & Reporting (Identical to H2H)			
Multiplicative noise std	σ_{mult}	0.1	log-scale
Overdispersion parameter	r	100	-
Reporting effects	-	Same as Table 2	various
Day-of-week effects	-	Same as Table 2	various
Lab noise parameters	-	Same as Table 2	various
Delay distributions	-	Same as Table 2	various

Key Differences from Other Transmission Modes

The waterborne simulator incorporates several distinguishing features:

Dual Transmission Pathways Unlike single-route models, waterborne diseases require simultaneous modeling of direct contact and environmental transmission, each with independent temporal dynamics and intervention susceptibilities.

Environmental Persistence The explicit water compartment captures pathogen persistence in the environment, creating temporal delays and amplification effects not present in direct transmission models.

Route-Specific Interventions Control strategies must address both transmission pathways, with water-focused interventions (treatment, sanitation) having different effectiveness profiles than contact-focused measures.

Enhanced Seasonal Dependence Environmental factors create stronger seasonal patterns than purely social transmission modes, reflected in increased amplitude ranges and environmental sensitivity.

Endemic Circulation Patterns Higher baseline immunity levels reflect the endemic nature of many waterborne diseases in affected populations, influencing outbreak dynamics and intervention effectiveness.

This comprehensive dual-route framework enables realistic simulation of waterborne disease dynamics across diverse environmental contexts, intervention strategies, and population immunity profiles, capturing the complex interplay between direct and indirect transmission pathways characteristic of environmentally-mediated pathogens.

B Model Architecture

Mantis is implemented as a hybrid convolutional-transformer architecture specifically designed for epidemiological time series forecasting. The model consists of five main components: (1) multi-scale input embeddings, (2) hybrid CNN-transformer encoder blocks, (3) an epidemic pattern memory bank, (4) an autoregressive quantile decoder, and (5) comprehensive temporal feature engineering. This section provides detailed specifications for each component.

B.1 Input Processing and Feature Engineering

B.1.1 Multi-Scale Convolutional Embedding

The input embedding layer processes time series data using parallel convolutions at multiple temporal scales to capture epidemiological patterns across different time horizons. For input tensor $\mathbf{X} \in \mathbb{R}^{B \times L \times 2}$ where B is

batch size, L is sequence length, and the feature dimension includes both target values and covariates (e.g., deaths and hospitalizations), the multi-scale embedding applies four parallel 1D convolutions:

$$\mathbf{H}_{\text{short}} = \text{Conv1D}(\mathbf{X}; k = 3, d_{\text{out}} = d/4) \quad (90)$$

$$\mathbf{H}_{\text{med}} = \text{Conv1D}(\mathbf{X}; k = 7, d_{\text{out}} = d/4) \quad (91)$$

$$\mathbf{H}_{\text{long}} = \text{Conv1D}(\mathbf{X}; k = 15, d_{\text{out}} = d/4) \quad (92)$$

$$\mathbf{H}_{\text{vlong}} = \text{Conv1D}(\mathbf{X}; k = 31, d_{\text{out}} = d/4) \quad (93)$$

where k denotes kernel size, d is the target hidden dimension (default 512), and each convolution uses appropriate padding to maintain sequence length. Each scale captures different temporal patterns:

- Short-term ($k=3$): Weekly variations and immediate trends
- Medium-term ($k=7$): Monthly patterns and intervention responses
- Long-term ($k=15$): Seasonal cycles and extended epidemic phases
- Very long-term ($k=31$): Annual seasonality and yearly trends

Each convolutional output is independently normalized and activated:

$$\tilde{\mathbf{H}}_i = \text{Dropout}(\text{SiLU}(\text{LayerNorm}(\mathbf{H}_i))) \quad \text{for } i \in \{\text{short, med, long, vlong}\} \quad (94)$$

The multi-scale features are concatenated and projected to the target hidden dimension:

$$\mathbf{H}_{\text{conv}} = \text{LayerNorm}(\mathbf{W}_{\text{proj}} \cdot \text{Concat}([\tilde{\mathbf{H}}_{\text{short}}, \tilde{\mathbf{H}}_{\text{med}}, \tilde{\mathbf{H}}_{\text{long}}, \tilde{\mathbf{H}}_{\text{vlong}}])) \quad (95)$$

where $\mathbf{W}_{\text{proj}} \in \mathbb{R}^{d \times d}$ is a learned projection matrix.

B.1.2 Static and Temporal Feature Embeddings

Mantis incorporates rich contextual information through multiple embedding layers:

Disease Type Embedding Disease categories are embedded using a learned lookup table:

$$\mathbf{e}_{\text{disease}} = \text{Embedding}(\text{disease_type}; |V| = 3, d_{\text{disease}} = 64) \quad (96)$$

where the three disease types correspond to human-to-human, waterborne, and vector-borne transmission modes from the training simulations.

Population Embedding Population size is processed through a multi-layer perceptron after log-normalization:

$$\mathbf{e}_{\text{pop}} = \text{GELU}(\text{LayerNorm}(\mathbf{W}_{\text{pop}} \cdot \log(1 + \text{population}))) \quad (97)$$

where $\mathbf{W}_{\text{pop}} \in \mathbb{R}^{64 \times 1}$ projects the scalar population to a 64-dimensional embedding.

Enhanced Temporal Embeddings Temporal patterns are captured through multiple cyclic embeddings derived from absolute day indices. For day index d_t at timestep t :

$$\mathbf{e}_{\text{dow}} = \text{LayerNorm}(\text{Embedding}(d_t \bmod 7; |V| = 7, d = 128)) \quad (98)$$

$$\mathbf{e}_{\text{month}} = \text{LayerNorm}(\text{Embedding}(\lfloor d_t/30 \rfloor \bmod 12; |V| = 12, d = 128)) \quad (99)$$

$$\mathbf{e}_{\text{doy}} = \text{LayerNorm}(\text{Embedding}(d_t \bmod 366; |V| = 366, d = 128)) \quad (100)$$

These embeddings capture day-of-week effects (reporting cycles), monthly seasonality, and annual patterns respectively.

B.1.3 Feature Integration

All embedding components are concatenated and projected to the model’s hidden dimension. Static embeddings are expanded across the temporal dimension:

$$\mathbf{H}_{\text{input}} = \text{LayerNorm}(\mathbf{W}_{\text{feat}} \cdot \text{Concat}([\mathbf{H}_{\text{conv}}, \mathbf{E}_{\text{disease}}, \mathbf{E}_{\text{pop}}, \mathbf{e}_{\text{dow}}, \mathbf{e}_{\text{month}}, \mathbf{e}_{\text{doy}}])) \quad (101)$$

where $\mathbf{E}_{\text{disease}}, \mathbf{E}_{\text{pop}} \in \mathbb{R}^{B \times L \times d_{\text{embed}}}$ are the temporally expanded static embeddings, and $\mathbf{W}_{\text{feat}} \in \mathbb{R}^{d \times (d+64+64+128+128+128)}$ projects the concatenated features to hidden dimension d .

B.2 Hybrid CNN-Transformer Encoder

The encoder consists of N stacked hybrid blocks (default $N = 16$), each combining local convolutional processing with global attention mechanisms.

B.2.1 Temporal Pattern Attention

Each encoder block uses a custom attention mechanism (‘TemporalPatternAttention’) that incorporates relative positional encoding specifically designed for temporal sequences:

$$\mathbf{Q}, \mathbf{K}, \mathbf{V} = \mathbf{HW}_Q, \mathbf{HW}_K, \mathbf{HW}_V \quad (102)$$

$$\mathbf{A}_{i,j} = \frac{\mathbf{Q}_i \mathbf{K}_j^T}{\sqrt{d_k}} + \mathbf{R}_{i-j+L-1} \quad (103)$$

$$\text{Attention}(\mathbf{H}) = \text{softmax}(\mathbf{A}) \mathbf{V} \quad (104)$$

where $\mathbf{R} \in \mathbb{R}^{2L-1 \times h}$ is a learned relative positional bias matrix with h attention heads, and $\mathbf{R}_{i-j+L-1}$ provides position-dependent bias for the attention score between positions i and j .

The relative positional encoding allows the model to learn temporal relationships that are translation-invariant, which is crucial for epidemiological patterns that may occur at different absolute times but with similar relative timing.

B.2.2 CNN-Transformer Hybrid Block

Each encoder block (‘CNNTransformerBlock’) follows a three-stage design with post-normalization:

Stage 1: Local Pattern Extraction

$$\mathbf{H}^{(1)} = \text{LayerNorm}(\mathbf{H}^{(0)} + \text{Dropout}(\text{LocalConv}(\mathbf{H}^{(0)}))) \quad (105)$$

where LocalConv applies depthwise separable convolution:

$$\text{LocalConv}(\mathbf{H}) = \text{Conv1D}(\text{DepthwiseConv1D}(\mathbf{H}; k = 5); k = 1) \quad (106)$$

The depthwise convolution (kernel size 5) captures local temporal dependencies within each feature channel, followed by a pointwise convolution that mixes information across channels.

Stage 2: Global Context Attention

$$\mathbf{H}^{(2)} = \text{LayerNorm}(\mathbf{H}^{(1)} + \text{Dropout}(\text{TemporalPatternAttention}(\mathbf{H}^{(1)}, \mathbf{M}))) \quad (107)$$

where $\mathbf{M} \in \{0, 1\}^{B \times L}$ is the padding mask indicating valid sequence positions.

Stage 3: Position-wise Feed-Forward

$$\mathbf{H}^{(3)} = \text{LayerNorm}(\mathbf{H}^{(2)} + \text{Dropout}(\text{FFN}(\mathbf{H}^{(2)}))) \quad (108)$$

where the feed-forward network is:

$$\text{FFN}(\mathbf{H}) = \mathbf{W}_2 \text{GELU}(\mathbf{W}_1 \mathbf{H} + \mathbf{b}_1) + \mathbf{b}_2 \quad (109)$$

with $\mathbf{W}_1 \in \mathbb{R}^{d \times d_{\text{ffn}}}$, $\mathbf{W}_2 \in \mathbb{R}^{d_{\text{ffn}} \times d}$, and $d_{\text{ffn}} = 2048$ by default.

B.3 Epidemic Pattern Memory Bank

The pattern memory module ('EpidemicPatternMemory') implements a learnable memory bank that stores prototypical epidemic patterns discovered during training.

B.3.1 Pattern Bank Initialization

The pattern bank consists of $K = 256$ learnable pattern vectors:

$$\mathbf{P} = [\mathbf{p}_1, \mathbf{p}_2, \dots, \mathbf{p}_K] \in \mathbb{R}^{K \times d} \quad (110)$$

Pattern vectors are initialized with small random values: $\mathbf{p}_k \sim \mathcal{N}(0, 0.02^2 \mathbf{I})$.

B.3.2 Pattern Matching and Retrieval

For encoder output $\mathbf{H}_{\text{enc}} \in \mathbb{R}^{B \times L \times d}$, pattern matching computes attention weights over the pattern bank:

$$\mathbf{S} = \text{FFN}_{\text{match}}(\text{LayerNorm}(\mathbf{H}_{\text{enc}})) \in \mathbb{R}^{B \times L \times K} \quad (111)$$

$$\mathbf{A}_{\text{pattern}} = \text{softmax}(\mathbf{S} \odot \mathbf{M}_{\text{exp}}) \quad (112)$$

$$\mathbf{H}_{\text{retrieved}} = \mathbf{A}_{\text{pattern}} \mathbf{P} \in \mathbb{R}^{B \times L \times d} \quad (113)$$

where $\mathbf{M}_{\text{exp}} \in \mathbb{R}^{B \times L \times 1}$ is the expanded padding mask, \odot denotes element-wise multiplication, and $\text{FFN}_{\text{match}}$ is a two-layer network:

$$\text{FFN}_{\text{match}}(\mathbf{x}) = \mathbf{W}_3 \text{GELU}(\mathbf{W}_4 \mathbf{x}) \quad (114)$$

with $\mathbf{W}_4 \in \mathbb{R}^{d \times d}$ and $\mathbf{W}_3 \in \mathbb{R}^{d \times K}$.

B.3.3 Pattern Integration

Retrieved patterns are projected and integrated with the encoder output using residual connections:

$$\mathbf{H}_{\text{memory}} = \text{LayerNorm}(\mathbf{H}_{\text{enc}} + \text{Dropout}(\mathbf{W}_{\text{proj}} \mathbf{H}_{\text{retrieved}})) \quad (115)$$

where $\mathbf{W}_{\text{proj}} \in \mathbb{R}^{d \times d}$ is a learned projection matrix.

B.4 Autoregressive Quantile Decoder

The decoder generates probabilistic forecasts using an autoregressive approach with a two-layer GRU and cross-attention to encoder memory.

B.4.1 Decoder Initialization

The decoder state is initialized using masked pooling of the encoder output:

$$\mathbf{h}_0 = \mathbf{W}_{\text{init}} \cdot \text{MaskedPool}(\mathbf{H}_{\text{memory}}, \mathbf{M}) \quad (116)$$

$$\text{MaskedPool}(\mathbf{H}, \mathbf{M}) = \frac{\sum_{t=1}^L \mathbf{M}_{:,t} \odot \mathbf{H}_{:,t,:}}{\sum_{t=1}^L \mathbf{M}_{:,t} + \epsilon} \quad (117)$$

where $\mathbf{W}_{\text{init}} \in \mathbb{R}^{d \times d}$ and $\epsilon = 10^{-10}$ prevents division by zero. The initial state is replicated for the two-layer GRU: $\mathbf{h}_0^{(1)} = \mathbf{h}_0^{(2)} = \mathbf{h}_0$.

B.4.2 Autoregressive Generation

For each forecast step $\tau \in \{1, 2, \dots, H\}$ where H is the forecast horizon:

Step 1: Input Processing The previous prediction $y_{\tau-1}$ is embedded:

$$\mathbf{e}_\tau = \text{GELU}(\text{LayerNorm}(\mathbf{W}_{\text{input}} y_{\tau-1})) \in \mathbb{R}^{B \times d/4} \quad (118)$$

Step 2: Cross-Attention The top GRU layer output attends to encoder memory:

$$\mathbf{q}_\tau = (\mathbf{h}_{\tau-1}^{(2)})^T \in \mathbb{R}^{B \times 1 \times d} \quad (119)$$

$$\mathbf{c}_\tau = \text{MultiHeadAttention}(\mathbf{q}_\tau, \mathbf{H}_{\text{memory}}, \mathbf{H}_{\text{memory}}, \neg \mathbf{M}) \quad (120)$$

where $\neg \mathbf{M}$ serves as the key padding mask (True for padded positions).

Step 3: GRU Update The concatenated input is processed through the two-layer GRU:

$$\mathbf{x}_\tau = \text{Concat}([\mathbf{c}_\tau, \mathbf{e}_\tau]) \in \mathbb{R}^{B \times 1 \times (d+d/4)} \quad (121)$$

$$\mathbf{h}_\tau^{(1)}, \mathbf{h}_\tau^{(2)} = \text{GRU}(\mathbf{x}_\tau, [\mathbf{h}_{\tau-1}^{(1)}, \mathbf{h}_{\tau-1}^{(2)}]) \quad (122)$$

Step 4: Quantile Prediction 23 quantiles are predicted using separate projection heads:

$$\hat{q}_\tau^{(i)} = \mathbf{W}_{\text{out}}^{(i)} \text{GELU}(\text{LayerNorm}(\mathbf{W}_{\text{hidden}}^{(i)} \mathbf{h}_\tau^{(2)})) \quad (123)$$

$$\text{for } i \in \{1, 2, \dots, 23\} \quad (124)$$

where each quantile head has parameters $\mathbf{W}_{\text{hidden}}^{(i)} \in \mathbb{R}^{(d/2) \times d}$ and $\mathbf{W}_{\text{out}}^{(i)} \in \mathbb{R}^{1 \times (d/2)}$.

The 23 quantiles are: [0.01, 0.025, 0.05, 0.1, 0.15, 0.2, 0.25, 0.3, 0.35, 0.4, 0.45, 0.5, 0.55, 0.6, 0.65, 0.7, 0.75, 0.8, 0.85, 0.9, 0.95, 0.975, 0.99].

B.4.3 Teacher Forcing

During training, teacher forcing is applied with linearly decaying probability:

$$p_{\text{tf}}(s) = p_{\text{initial}} \cdot \left(1 - \frac{s}{S_{\text{total}}}\right) + p_{\text{final}} \cdot \frac{s}{S_{\text{total}}} \quad (125)$$

where s is the current training step, S_{total} is the total number of training steps, $p_{\text{initial}} = 0.2$, and $p_{\text{final}} = 0.0$.

At each step, with probability $p_{\text{tf}}(s)$, the true target value is used as input instead of the model's prediction:

$$y_\tau = \begin{cases} \text{target}_\tau & \text{if } U(0, 1) < p_{\text{tf}}(s) \text{ and training} \\ \hat{q}_\tau^{(5)} & \text{otherwise (median prediction)} \end{cases} \quad (126)$$

B.5 Training Configuration

B.5.1 Weight Initialization

Model parameters are initialized using a careful scheme to ensure stable training:

$$\mathbf{W}_{\text{linear}} \sim \text{Xavier uniform with gain 0.01} \quad (127)$$

$$\mathbf{b} = \mathbf{0} \quad (128)$$

$$\mathbf{E}_{\text{embedding}} \sim \mathcal{N}(0, 0.01^2) \quad (129)$$

$$\mathbf{P}_{\text{pattern}} \sim \mathcal{N}(0, 0.02^2) \quad (130)$$

B.5.2 Loss Function

The model is trained using quantile loss (pinball loss) averaged across all quantiles:

$$\mathcal{L}_{\text{quantile}} = \frac{1}{BH|Q|} \sum_{b=1}^B \sum_{\tau=1}^H \sum_{q \in Q} \rho_q(y_{b,\tau} - \hat{q}_{b,\tau}^{(q)}) \quad (131)$$

$$\rho_q(e) = \max(qe, (q-1)e) \quad (132)$$

where $Q = \{0.05, 0.1, 0.25, 0.4, 0.5, 0.6, 0.75, 0.9, 0.95\}$ is the set of quantile levels, and e is the prediction error.

B.5.3 Optimization

The model is trained using AdamW optimizer with OneCycle learning rate scheduling:

$$\text{AdamW} : \beta_1 = 0.9, \beta_2 = 0.999, \text{weight decay} = 0.01 \quad (133)$$

$$\text{OneCycle} : \text{max_lr} = 10^{-4}, \text{pct_start} = 0.05, \quad (134)$$

$$\text{div_factor} = 10.0, \text{final_div_factor} = 100.0 \quad (135)$$

Gradient clipping is applied with maximum norm 1.0, and training uses gradient accumulation every 64 steps to simulate larger effective batch sizes.

B.6 Model Scale and Efficiency

The full model configuration uses:

- Hidden dimension: $d = 1024$
- Feed-forward dimension: $d_{\text{ffn}} = 2048$
- Number of encoder layers: $N = 16$
- Number of attention heads: $h = 16$
- Pattern memory size: $K = 256$
- Total parameters: approximately 150M

Training requires approximately 2 days on a single NVIDIA L4 GPU for one complete pass through the synthetic dataset (we only train with one epoch, since we can generate as much data as we need), while inference can be performed in real-time on standard hardware.

C Evaluation Data

After training, Mantis is evaluated on real-world forecasting tasks spanning multiple diseases, regions, and targets. For each task, the model is run out-of-the-box: no retraining, fine-tuning, or exposure to real data is performed. Forecast accuracy is assessed using both pointwise metrics such as mean absolute error (MAE), weighted interval score (WIS), and coverage metrics. Mantis’s performance is compared to established forecasting benchmarks, including the CDC Forecast Hub ensemble and individual submissions [2], as well as published models such as Chronos [18].

C.1 Primary Evaluation Tasks

C.1.1 COVID-19 Mortality Across U.S. States

To assess generalization to novel outbreak scenarios, we evaluated Mantis on weekly COVID-19 death forecasts across all 50 U.S. states, the District of Columbia, and Puerto Rico during the first two years of the pandemic (April 2020 through November 2021). This evaluation period matches the timeframe used in [2], enabling direct comparison with published CDC COVID-19 Forecast Hub results.

Data Characteristics

- **Temporal Coverage:** Weekly data from April 2020 through November 2021 (87 weeks)
- **Geographic Resolution:** 52 jurisdictions (50 states + DC + Puerto Rico)
- **Outcome Variable:** Weekly COVID-19 deaths
- **Population Range:** 580,000 (Wyoming) to 39.5 million (California)
- **Total Forecasts:** Approximately 22,776 individual forecasts across all jurisdictions and horizons
- **Data Source:** CDC COVID-19 surveillance data [12]

Baseline Comparisons We benchmarked against models from the U.S. CDC COVID-19 Forecast Hub, which represented expert-curated approaches from modeling teams throughout the pandemic:

- **CDC Forecast Hub ensemble:** Weighted combination of top-performing individual models
- **Individual Hub models:** 28 distinct modeling approaches including statistical, mechanistic, and machine learning methods
- **Covariate utilization:** Most models incorporated extensive covariate information including case counts, mobility data, and syndromic surveillance signals
- **Continuous retraining:** Baselines were retrained as new data became available, reflecting operational practice

C.2 Distribution Shift Evaluation Tasks

To further assess generalization capabilities under varying degrees of distribution shift, we conducted four additional evaluations on diseases and contexts that challenge different aspects of model robustness.

C.2.1 Dengue Fever in Brazil (Vector-Borne Transmission)

We evaluated Mantis on dengue fever case forecasting across Brazilian states from 1993 to 2005, representing real-world vector-borne transmission dynamics within the model’s training distribution.

Data Characteristics

- **Temporal Coverage:** Monthly data from 1993 through 2005 (156 months)
- **Geographic Resolution:** Alagoas, Brazil
- **Outcome Variable:** Monthly dengue fever cases
- **Population Range:** Roughly 3 million
- **Total Forecasts:** Approximately 4,096 individual forecasts
- **Data Source:** Project Tycho [13]
- **Transmission Mode:** Vector-borne (included in training simulations)

C.2.2 Scarlet Fever in the United States (Historical Context)

Scarlet fever forecasting across U.S. states from 1910 to 1950 represents historical surveillance contexts with limited infrastructure and irregular reporting patterns.

Data Characteristics

- **Temporal Coverage:** Weekly data from 1910 through 1950 (40 years)
- **Geographic Resolution:** 48 contiguous U.S. states (Alaska and Hawaii not yet states)
- **Outcome Variable:** Weekly scarlet fever cases
- **Population Range:** 200,000 to 10 million per state (1910-1950 demographics)
- **Total Forecasts:** Approximately 70,560 individual forecasts
- **Data Source:** Project Tycho [16]
- **Distribution Shift:** Early 20th-century surveillance systems with limited medical infrastructure

C.2.3 Hepatitis B in the United States (Blood-Borne Transmission)

Hepatitis B forecasting across U.S. states from 1978 to 1988 represents chronic blood-borne infections with long latency periods—a transmission mode explicitly excluded from Mantis’s training data.

Data Characteristics

- **Temporal Coverage:** Weekly data from 1978 through 1988 (11 years)
- **Geographic Resolution:** 50 U.S. states
- **Outcome Variable:** Weekly hepatitis B cases
- **Population Range:** 400,000 to 25 million per state (1980s demographics)
- **Total Forecasts:** Approximately 57,344 individual forecasts
- **Data Source:** Project Tycho [14]
- **Distribution Shift:** Chronic blood-borne transmission not included in training simulations

C.2.4 Smallpox in the United States (Eradicated Disease)

Smallpox forecasting across U.S. states from 1925 to 1933 represents an eradicated disease with no modern analog in the training dataset.

Data Characteristics

- **Temporal Coverage:** Weekly data from 1925 through 1933 (9 years)
- **Geographic Resolution:** 48 contiguous U.S. states
- **Outcome Variable:** Weekly smallpox cases
- **Population Range:** 500,000 to 12 million per state (1920s-1930s demographics)
- **Total Forecasts:** Approximately 21,888 individual forecasts
- **Data Source:** Project Tycho [15]
- **Distribution Shift:** Eradicated disease with no training analog; pre-vaccine era dynamics

C.2.5 Influenza-Like Illness (ILI) in the United States (Syndromic Data)

ILI forecasting across U.S. states from 2013 to 2025 represents a challenge to Mantis due to the lack of syndromic indicators in its training set.

Data Characteristics

- **Temporal Coverage:** Weekly data from 2013 through 2025 (13 years) [10]
- **Geographic Resolution:** 50 U.S. states, Washington D.C., and Puerto Rico.
- **Outcome Variable:** Weekly percentage of outpatient visits due to ILI.
- **Population Range:** 500,000 to 40 million per state
- **Total Forecasts:** Approximately 35,000 individual forecasts
- **Data Source:** CMU DELPHI [11]
- **Distribution Shift:** Syndromic indicator is a data type not seen during training

C.3 Baseline Model Implementations

For the distribution shift evaluation tasks, we implemented strong statistical baselines to establish performance benchmarks:

C.3.1 Naïve Persistence Model

The persistence model assumes that future values will equal the most recent observed value:

$$\hat{y}_{t+h} = y_t \quad \text{for all forecast horizons } h \quad (136)$$

C.3.2 Exponential Smoothing (ETS)

We implemented exponential smoothing models with optimal configuration selection via Akaike Information Criterion (AIC). For each disease and forecast window, we evaluated a comprehensive range of ETS variants:

- **Error types:** Additive and multiplicative
- **Trend types:** None, additive, additive damped, multiplicative, multiplicative damped
- **Seasonal types:** None, additive, multiplicative
- **Training procedure:** Rolling forecasts with 104 weeks (or maximum available) of historical context
- **Model selection:** Best configuration selected per disease based on AIC across training period

C.3.3 Seasonal ARIMA (SARIMA)

We implemented seasonal autoregressive integrated moving average models with automatic order selection. For each disease and forecast window, the model specification was determined using the following procedure:

- **Order selection:** Auto ARIMA algorithm to determine optimal $(p, d, q) \times (P, D, Q)_s$ parameters based on AIC
- **Seasonality:** Period determined by data frequency (e.g., 52 for weekly)
- **Training procedure:** Model refit at each time step using all available historical data up to the forecast origin
- **Forecast generation:** Rolling forecasts with the refitted model producing multi-step-ahead predictions
- **Model selection:** Best SARIMA specification selected per disease based on AIC performance during the initial training period

C.3.4 Long Short-Term Memory Network (LSTM)

We implemented a deep recurrent neural network baseline using a multi-layer LSTM architecture. The model was retrained at each forecast point to incorporate all available historical data:

- **Architecture:** 6-layer LSTM with hidden dimension of 128 units per layer
- **Regularization:** Dropout rate of 0.5 applied between LSTM layers
- **Data preprocessing:** Standard scaler applied to normalize input time series
- **Training procedure:** Model retrained from scratch at each time step using all available historical data
- **Training duration:** 50 epochs per retraining with early stopping based on validation loss
- **Forecast generation:** Rolling forecasts produced after retraining at each forecast origin

C.4 Data Preprocessing and Quality Control

C.4.1 Standardization

All time series were preprocessed using consistent procedures:

- **Missing value handling:** Linear interpolation for isolated missing points; exclusion of series with $\geq 10\%$ missing data (this leads to most states being excluded for the historical diseases)
- **Minimum length requirements:** Series with ≤ 52 observations excluded from evaluation

C.4.2 Forecast Windows

Evaluation employed rolling forecast windows with consistent protocols:

- **Context length:** Up to 112 weeks of historical data for model input
- **Forecast horizons:** 4 and 8 weeks ahead for primary tasks; 8 weeks for distribution shift tasks
- **Rolling evaluation:** New forecasts generated weekly/monthly as new data became available
- **Evaluation metrics:** Mean Absolute Error (MAE), Mean Absolute Percentage Error (MAPE), 90% prediction interval coverage

C.5 Evaluation Scope Summary

Table 5 summarizes the complete evaluation framework, highlighting the diversity of diseases, transmission modes, geographic scales, and temporal contexts covered in our assessment.

Table 5: Summary of Mantis Evaluation Framework

Disease	Location	Period	Frequency	Transmission	Distribution Shift
Influenza	Michigan regions	2023-2024	Weekly	Respiratory	None (in-distribution)
COVID-19	U.S. states/territories	2020-2021	Weekly	Respiratory	Novel pathogen
Dengue	Brazilian states	1993-2005	Monthly	Vector-borne	None (in-distribution)
Scarlet fever	U.S. states	1910-1950	Annual	Respiratory	Historical context
Hepatitis B	U.S. states	1978-1988	Annual	Blood-borne	Excluded transmission
Smallpox	U.S. states	1925-1933	Annual	Respiratory	Eradicated disease

This comprehensive evaluation framework enables robust assessment of Mantis’s forecasting capabilities across the full spectrum of infectious disease scenarios, from routine seasonal diseases to novel outbreaks and historically eradicated pathogens. The combination of primary tasks (representing operational forecasting scenarios) and distribution shift challenges (testing model robustness) provides a thorough evaluation of the simulation-grounded approach’s generalization capabilities.

D Additional Results

D.1 Ablation Studies Confirm the Importance of Scale and Mechanistic Pre-training

To understand the key factors driving Mantis’s performance, we conducted two ablation studies examining the roles of architectural capacity and mechanistic pretraining in enabling accurate plug-and-play forecasting.

D.1.1 Architectural Capacity Requirements

We first evaluated whether Mantis’s forecasting capabilities could be achieved with a simpler, more compact architecture. Using the same 400 million days of synthetic training data, we replaced Mantis’s hybrid CNN-transformer architecture with the dual-branch LSTM architecture from DEFSI [9]. This LSTM model contains approximately 200 times fewer parameters than Mantis, making it significantly more lightweight and computationally efficient.

Despite identical training data and procedures, the reduced architectural capacity led to substantially degraded performance. When evaluated on COVID-19 mortality forecasting across U.S. states, the LSTM architecture achieved mean absolute error (MAE) that was 89% higher than the full Mantis model. This demonstrates that while the synthetic training paradigm is powerful, it requires sufficient architectural capacity to effectively learn and generalize from the diverse mechanistic patterns encoded in the simulation data.

D.1.2 Mechanistic Pretraining is Essential for Novel Outbreak Performance

To isolate the contribution of mechanistic pretraining, we trained the full Mantis architecture exclusively on real-world data, eliminating simulations from the training process. We evaluated on COVID-19 hospitalization forecasting. We implemented a rolling training strategy that provided the strongest possible baseline: the model was initially trained on the first few months of pandemic data, then progressively retrained with expanding datasets as more real-world observations became available. This approach mimics operational practice and ensures that the real-world-only model has access to all available historical information at each forecast point.

The results reveal the critical importance of mechanistic pretraining. When trained only on real-world COVID-19 data, forecast error increased by 262% compared to the simulation-pretrained Mantis model. This dramatic performance degradation reflects the fundamental challenge of learning outbreak dynamics

from limited historical data during a novel pandemic. Real-world training data, even when accumulated over months, cannot capture the full spectrum of epidemic behaviors that might emerge. In contrast, the simulation-pretrained model draws from hundreds of millions of days of diverse outbreak scenarios, enabling it to recognize and extrapolate patterns even in unprecedented contexts.

These ablation results underscore the core insight behind Mantis: mechanistic pretraining enables models to internalize generalizable principles of epidemic dynamics that extend far beyond what can be learned from any single real-world outbreak. While architectural sophistication contributes to performance, the simulation-grounded training paradigm is the essential component that enables out-of-the-box generalization to novel diseases and outbreak contexts.

D.2 Performance Consistency Across Population Scales

To assess whether Mantis’s performance varies systematically with jurisdiction size, we analyzed the relationship between state population and forecast accuracy for the COVID-19 mortality forecasting task. We computed the mean relative MAE for each U.S. state and territory across all forecast dates in the evaluation period (April 2020 through November 2021) and examined the correlation with 2020 Census population estimates.

Figure 4 shows Mantis’s relative MAE versus state population on a logarithmic scale. We excluded Vermont from this analysis due to anomalous worse performance, perhaps due to data quality issues: in Vermont’s COVID-19 surveillance data, hospitalizations significantly lag deaths (rather than preceding them as expected), suggesting potential reporting artifacts that confound model evaluation. Among the remaining 51 jurisdictions, we observed a weak negative correlation between log population and relative MAE ($R^2 = 0.06$), meaning Mantis performs slightly better in larger states. However, the low R^2 value suggests that Mantis performance is relatively consistent across diverse population scales.

This consistency is positive given that smaller jurisdictions present distinct forecasting challenges due to noisier case trajectories and sometimes less available data. The weak relationship between population and performance suggests that Mantis’s simulation-based training enables robust forecasting across the spectrum of population sizes from states like Wyoming to California.

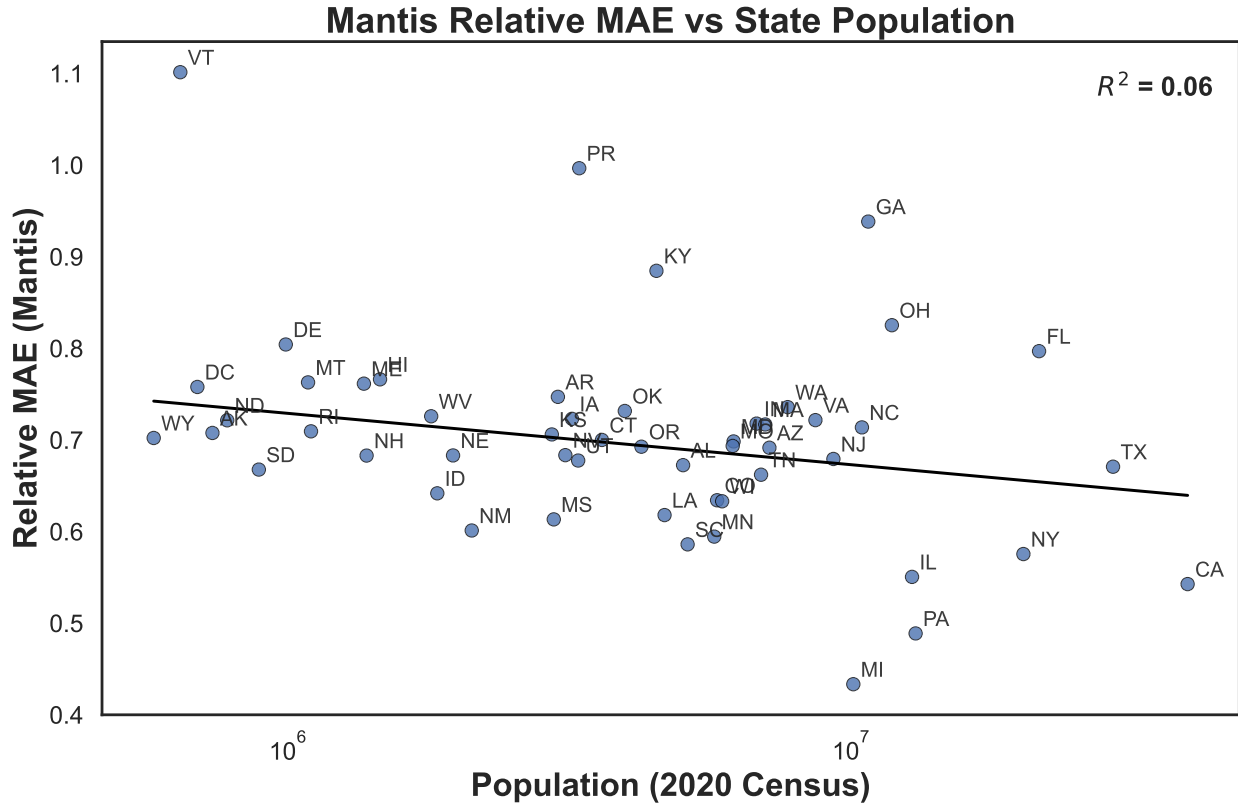


Figure 4: **Mantis delivers consistent performance across population scales.** Relative MAE versus state population for COVID-19 mortality forecasts across 51 U.S. states and territories (Vermont excluded as an outlier). Each point represents the mean relative MAE for a jurisdiction across all forecast dates from April 2020 through November 2021. Population is shown on a logarithmic scale (2020 Census). A weak negative correlation ($R^2 = 0.06$) indicates slightly better performance in larger states, but the low coefficient of determination suggests that Mantis achieves relatively uniform accuracy across diverse population sizes.